REVIEW ARTICLE

physica status solidi b
www.pss-b.com
Check for updates

Defect-Induced Magnetism in Nonmagnetic Oxides: Basic Principles, Experimental Evidence, and Possible Devices with ZnO and TiO$_2$

Pablo David Esquinazi,* Wolfram Hergert, Markus Stiller, Lukas Botsch, Hendrik Ohldag, Daniel Spemann, Martin Hoffmann, Waheed A. Adeagbo, Angelika Chassé, Sanjeev K. Nayak, and Hichem Ben Hamed

The magnetic moment and the magnetic order induced by localized defects, like vacancies, interstitials, and/or nonmagnetic (NM) ions, in a NM oxide atomic lattice are discussed. When the defect concentration is of the order of or larger than ≈3 at%, magnetic order at room temperature can appear. Herein, the theoretical basic principles needed to understand and compute this new magnetic phenomenon in solids are developed in detail. In particular, the main results of density functional theory (DFT) calculations are used to estimate the magnetization and X-ray magnetic circular dichroism (XMCD) values. The main experimental evidences on this phenomenon are reviewed, especially magnetization, the element-specific XMCD, and transport properties in two selected oxides, ZnO and TiO$_2$. Emphasis is given on the simplicity and efficiency ion irradiation methods have to trigger magnetic order in these oxides as well as a very sensitive method to characterize magnetic impurities. Two possible applications of this phenomenon are discussed, namely spin filtering at magnetic/NM interfaces in ZnO and perpendicular magnetic anisotropy triggered in TiO$_2$ anatase microstructures. The existing literature on defect-induced magnetism in oxides is shortly reviewed, which provides further evidence on the robustness of this phenomenon in solids.

1. Introduction

Nowadays, the magnetic properties of solids play a main role in different kinds of applications. In particular, magnetic order, like ferromagnetism (FM) or antiferromagnetism (AFM), is a phenomenon that attracts the interest of a large scientific community. From the materials research side, there is still the need of new materials with magnetic order above room temperature (RT). Interestingly, although there are a large number of magnetic compounds including oxides with ordering temperatures above RT (especially with transition metals like Fe, Co, Ni, etc.), its percentage with respect to the total number of magnetically ordered materials remains rather small. From the theoretical side, magnetic order still belongs to one of the most complex phenomena in solid-state physics. Its origin is given by the exchange interaction, a quantum mechanical mechanism

Prof. P. D. Esquinazi, M. Stiller, L. Botsch
Division of Superconductivity and Magnetism
Felix Bloch Institute for Solid State Physics
University of Leipzig
Leipzig 04103, Germany
E-mail: esquin@physik.uni-leipzig.de

Prof. W. Hergert, Dr. W. A. Adeagbo, Dr. A. Chassé, H. Ben Hamed
Institute of Physics
Martin Luther University Halle-Wittenberg
Halle 06120, Germany

Prof. H. Ohldag
Advanced Light Source
Lawrence Berkeley National Laboratory
Berkeley, CA 94720, USA

The ORCID identification number(s) for the author(s) of this article can be found under https://doi.org/10.1002/pssb.201900623.

Prof. H. Ohldag
Department of Material Science and Engineering
Stanford University
Stanford, CA 94305, USA

Prof. H. Ohldag
Department of Physics
University of California Santa Cruz
Santa Cruz, CA 95064, USA

Dr. D. Spemann
Ion Source Development and Application Group
Leibniz Institute of Surface Engineering (IOM)
Leipzig 04318, Germany

Dr. M. Hoffmann
Institute for Theoretical Physics
Johannes Kepler University Linz
Linz 4040, Austria

Dr. S. K. Nayak
Department of Materials Science & Engineering
Institute of Materials Science
University of Connecticut
Storrs, CT 06269, USA

between electron spins from nearest neighbors in the atomic lattice that determine the probability of alignment (or antialignment). The exchange interaction, whose strength is usually given by the exchange constant J, is basically a Coulomb interaction including the Pauli principle. The exchange interaction concept was introduced by Heisenberg in his work published in the city of Leipzig (Germany) in 1928, entitled "Zur Theorie des Ferromagnetismus."[1] This new concept on the magnetic pairing between nearest neighbors magnetic moments triggered a large number of research, opening up a fascinating and important development in solid-state physics, particularly in magnetism.

In his concluding remarks of the 1928 article, Heisenberg wrote explicitly that a necessary condition to trigger magnetic order in solids is that the principal quantum number n of the involved ions should be $n \gtrsim 3$, ruling out atoms that form crystals with s and p electronic bands only. Furthermore, ions of the atomic lattice with full d- or f-shells were not expected to directly contribute to any magnetic order. The success of this concept added to Hund's rules to estimate the magnetic moments of ions in solids established the main pillar of magnetism in solids. Because of its success but also due to some technical restrictions, the Heisenberg view left no room to accept that magnetic order at RT can occur in solids without any magnetic ions or with ions with s and p electrons only. It took a long time till systematic ferromagnetic signals at RT in carbon-based materials (mainly graphite based) were published (see, e.g., the review by Esquinazi[2]). Slowly, researchers started to recognize the intrinsic nature of the phenomenon called nowadays defect-induced magnetism (DIM). This phenomenon is found not only in carbon-based[3,4] but also in a large number of materials, including oxides, the class of materials that we discuss in this work. Several reviews were published on this topic in the past decade.[5–9]

We would like to note that the development of DIM in oxides is correlated with the one of the so-called "diluted magnetic semiconductors" (DMS). This name refers to semiconducting materials, like ZnO, where a magnetic order was predicted to occur upon doping with a relatively low amount of magnetic ions in 2000.[10] The expectations of the DMS as possible candidates for magneto-electric-optic devices were very large, and a significant amount of efforts were invested in the years after, also in theoretical investigations.[11] However, either the Curie temperature remained clearly below 300 K (e.g., Mn–GaAs[12]) or unclear or contradictory results in some magnetically doped semiconductors casted doubt on the origin of the magnetic order, see, e.g., the studies by Neal et al.[13] and Gacic et al.[14] For recent reviews, see the studies by Prellier et al.[15] and Dietl and Ohno.[16] Systematic measurements clarified to some extent[17–19] that the observed magnetic order at RT is related to defects and not necessarily to the magnetic-ion doping, similar to the main paradigm of DIM, namely graphite.[9,20,21]

While in conventional magnetically ordered materials the magnetic moments in the atomic lattice are directly related to the d- or f-unfilled electronic shells, the localized magnetic moments induced by defects can have different origins due to the large variety of atomic lattice defects and lattice structures. Moreover, we still do not have the necessary tools equivalent to "Hund's rules" to predict the magnitude of the magnetic moment for a given atomic lattice defect (from now on, we use simply the word "defect").

Pablo D. Esquinazi received his Ph.D. in physics in 1983 at the Instituto Balseiro in Bariloche, Argentina. After a Post-doc stay at the ICTP in Trieste, Italy, at the Institute for Applied Physics II at Heidelberg University, Germany, and at the Low-Temperature Physics Laboratory at the Centro Atómico Bariloche, he got an academic position in 1988 finishing his habilitation (Frank Pobell group) at the University of Bayreuth, in 1991. In 1994, he became a full professor at the University of Leipzig and head of the Superconductivity and Magnetism Division of the Faculty of Physics and Earth Sciences.
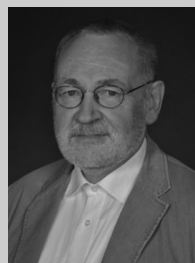
Wolfram Hergert received his Ph.D. in the field of solid-state theory in 1982 at Martin Luther University Halle-Wittenberg, Germany. After habilitation in 1989, he was appointed as extraordinary professor for computational physics. Main subjects of his work are group theory applications in solid-state theory, electronic and magnetic structures of nanostructure and photonics.

Markus Stiller is a Ph.D. student at the University of Leipzig, Germany, and works in the Division of Superconductivity and Magnetism on his Ph.D. His work focuses on DIM in oxides, in particular, in titanium dioxide, and their implementation in devices such as magnetic storage or semiconductor devices.

In addition to this theoretical problem, we have always an uncertainty in the magnetic defects density produced in the samples by means of a certain experimental procedure. Methods such as positron annihilation, high-resolution X-ray absorption spectroscopy (XAS), infrared absorption, Raman spectroscopy, Monte–Carlo (MC) simulations after ion irradiation, and others can help reduce to a certain extent this uncertainty. Although the characterization methods of defects, like native point defects in semiconductors and especially in nanostructures,[22] are continuously improving, the problem of determining which defect can produce a finite magnetic moment and how large it might be still remains.

While there is little doubt on the density of a certain magnetic ion in an usual magnetic compound, we cannot in general affirm the same for the magnetic defect density. Admittedly, this makes any comparison between predicted and experimental values difficult. Nevertheless, we will show in this Review a few experimental cases, where this uncertainty can be satisfactorily reduced by systematically creating a certain defect density, distributed

1900623 (2 of 29)

homogeneously and at random, maybe within a certain depth inside a sample, by light-ion irradiation. We will not discuss in detail the RT magnetism reported in undoped oxides due to, e.g., grain boundaries[23–25] or purely surface-located magnetism,[26] as a systematic treatment of the defect densities is less obvious in these cases. In contrast, ion irradiation allows to reproducibly create a certain defect density and trigger DIM in a controlled way, which is necessary for its applications. Two examples of possible applications of DIM in the two selected oxides are described and discussed in Section 4.

Before we discuss the ZnO and TiO$_2$ compounds, we would like to show a few, simple examples of defects in a nominally nonmagnetic (NM) oxide lattice. For a review on defects in ZnO, see the study by McCluskey and Jokela.[27] There are several basic questions that need an answer, experimentally and theoretically. For example,

1) Could a single vacancy (at the cation or anion site) have a significant magnetic moment (of the order of $m \gtrsim 0.1\,\mu_B$, where μ_B is the Bohr magneton)? **Figure 1**a shows a simple 2D oxide lattice of the type MO, where M is the cation and O the oxygen atom. This lattice is equivalent to 2D planes of MgO or CaO (or without taking care of the real lattice structure also to ZnO). One may speculate that the remaining dangling bonds of the neighboring oxygen atoms to the vacancy can end with a finite magnetic moment. Indeed, most of the experimental and

theoretical works indicate the existence of a significant magnetic moment when the cation place is empty. Theoretical work indicates that dilute divalent cation vacancies in oxides with rocksalt structure lead to a ferromagnetic ground state with a spin triplet state.[28] This result appears to be also applicable to other compounds with vacancies in octahedral coordination. As for the DIM in ZnO concerns, there is consent that the main results, which we partially discuss in this Review including X-ray-based microscopy and spectroscopy analyses, indicate that the magnetic order can be unambiguously attributed to the O 2p orbitals arising from zinc vacancies. This does not apply for DIM in TiO$_2$ with Ti vacancies, as we will discuss in this Review. In addition, there is consent that an oxygen vacancy V_O in undoped ZnO does not trigger a significant magnetic moment.[29] However, in case of doped ZnO with NM elements, there are other defects or defective structures, like in case (4) discussed later, where oxygen vacancies may play a role in the coupling between magnetic moments localized at the foreign ion. Theoretically, the estimate of the magnetic moment is not straightforward because the neighboring oxygen atoms shift without the cation atom outward (as indicated by the red arrows in Figure 1b) and one has a new local symmetry with not always well-known distortions. These distortions might be significant due to the exponential dependence of the exchange interaction coupling on the distance. Most of the published studies conducted in ZnO indicate the existence of a finite magnetic moment at the Zn vacancy (V_{Zn}). As a result of calculations by means of density functional theory (DFT), cation vacancies in ZnO carry a magnetic moment of $\approx 2.0\,\mu_B$.[30] The magnetic interaction of such defects breaks down if localization corrections[31] are considered. Interestingly, most of the published works do not support the existence of an AFM state in this case. The effects of vacancies at the surface of oxides are more difficult to predict due to the obvious asymmetry of the problem and the different possible terminations. In case of oxygen-terminated ZnO(001) surface, RT p-induced surface FM is expected.[32]

2) The possible influence of hydrogen in the magnetism of ZnO requires an extra paragraph. The effects of hydrogen bonded on the polar Zn-ended ZnO(0001) surface on magnetism and metallicity were studied in detail in the study by Sanchez et al.[33] The hydrogen-induced metallization was confirmed by angular-resolved photoelectron spectroscopy (ARPES), not only in the predicted termination but also on ZnO(10$\bar{1}$0) and O-terminated ZnO(000$\bar{1}$).[34] Its influence on (near-surface region) magnetism at RT observed in certain H$_2$-treated or H$^+$-irradiated ZnO samples was shown experimentally in several studies.[35–39] The presence of hydrogen is unavoidable in all systems, and it is difficult to measure it with high enough accuracy. The role of hydrogen in ZnO can be diverse, acting as donor (H$^+$) or acceptor (H$^-$) or even modifying the host structure. It is one source of the unintentional n-type conductivity.[40] Some of the published results will be discussed in Section 3.2.1 and 3.2.2. We would like to point out now that even when the FM induced by hydrogenation in ZnO can be switched "on" and "off" through particular treatments, it does not necessarily mean that H alone takes active part in triggering the magnetic moments or making a coupling between them. For example, using X-ray photoelectron spectroscopy and positron annihilation spectroscopy (PAS) analyses, Xue et al.[41] showed that V_{Zn} and an OH bonding complex
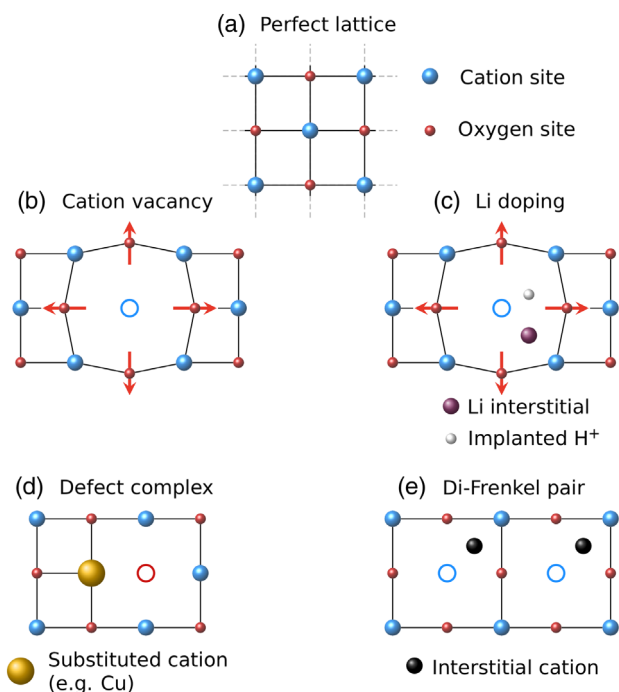

Figure 1. Sketch of possible atomic lattice defects within an oxide lattice that can produce localized magnetic moments in an otherwise nonmagnetic lattice. A square lattice is used for simplicity (blue—cations, like Zn, Mg, Ti, and so on, red—oxygen). a) Structure without defects, b) cation vacancy, c) Li doping with interstitial H$^+$ (red arrows stand for relaxations around the vacancy), d) defect complex consisting of substituted cation and oxygen vacancy (red open circle), e) di-FP. The cases (d,e) are drawn without lattice relaxations for clarity.

ADVANCED
SCIENCE NEWS

www.advancedsciencenews.com

physica pssb
status solidi

www.pss-b.com

(V_{Zn} + OH) were the source for the observed magnetic order at RT in ZnO nanoparticles. Previously, OH complexes at the surface of ZnO thin films were also proposed to be one cause for the observed RT magnetic order in H_2-treated ZnO films.[39]

3) One of the problems to produce a given density of cation vacancies, even if we use soft-ion irradiation methods to produce them, is that their density will not necessarily remain constant at RT because part of the vacancies can diffuse to the surface. In this case, DIM will not be stable at least at high temperatures. One possible solution, see Figure 1c, which was successfully tested,[42,43] is to use NM interstitials like Li or Na in the case of ZnO.[44] By implanting H^+ at low energies into Li-doped ZnO, one can solve two experimental problems in ZnO, namely, the concentration of V_{Zn} produced by low-energy H+ implantation will be of the order of the doped Li concentration without disturbing too much the ZnO lattice and the implanted H^+ generates the necessary defect complexes that stabilize the concentration of V_{Zn}. In other words, the defect complex V_{Zn}–Li–H^+ is stable at RT and has a finite magnetic moment of the order of $2\,\mu_B$.[43]

4) Could an NM foreign atom (like C, Cu, etc.) in a nominally NM oxide lattice trigger a localized magnetic moment and eventually magnetic order? Figure 1d shows the case where the foreign atom is in place of the cation near an oxygen vacancy. In the case of Cu, a certain amount of magnetic Cu^{2+} ions can appear near an oxygen vacancy. One of the first experimental and theoretical works on this Cu–V_O lattice defect was done in Cu-doped TiO_2 thin films.[45] The authors obtained a magnetic moment of $\simeq 1.5\,\mu_B$ per Cu atom. Their theoretical analysis indicates that this magnetic moment appears only if an oxygen vacancy in the nearest neighbor shell of Cu is present, stressing the role of oxygen vacancies to trigger FM in this case.[45] With a large concentration of Cu and V_O one may obtain a stable FM state at RT, with an extremely high Curie temperature of $T_C \approx 750\,K$, as shown in the study by Herng et al.[46] These results, however, were not completely reproduced in Cu-doped ZnO thin films prepared by pulsed laser deposition (PLD) and characterized by magnetometry, high-resolution X-ray diffraction (XRD), and X-ray magnetic circular dichroism (XMCD).[47] Although the films were ferromagnetic, the authors did not find clear signatures for a local magnetic moment associated with the Cu atoms. They argued that other "changes'' produced by doping are responsible for the magnetic order.[47] The recently published results of Cu-doped ZnO[48] thin films prepared by atomic beam cosputtering support the observed enhancement of the ferromagnetic response with Cu content, and the authors attributed it to the generation of large defects, such as the presence of oxygen vacancies, structural inhomogeneity, as well as formation of bound magnetic polarons. These examples already demonstrate that, in a given oxide lattice structure, with NM doping, together with certain defects, a rather unexpected magnetic state can appear, whereas its origin may depend on sample preparation details.

5) The examples (1)–(4) are some of several others in solids with DIM, some of which we discuss in this work. Clearly, the fact that a magnetic moment can be created in a nominally NM lattice, simply by introducing atomic lattice defects, is a completely new way to produce magnetism in solids. However, how large should be usually the necessary density of a given defect to trigger magnetic order at RT? After more or less

15 years of research, one can answer that the defect concentration necessary to trigger magnetic order above 300 K should be of the order of ≈ 3–$\approx 8\%$. Lower densities of defects can decrease substantially the Curie temperature below which an FM state is stable. Larger densities can destabilize the atomic lattice and new lattice structures, even amorphous ones, may appear. According to experimental results, amorphous oxides or amorphous carbon compounds (without magnetic ions) are not FM but, if at all, paramagnetic (PM).

6) Assuming now that an oxide has a significant density of defects, and each defect possesses a finite magnetic moment, large enough to sum altogether a net magnetization at saturation $M_s \gtrsim 10\,emug^{-1}$ (e.g., pure Ni has $\approx 40\,emug^{-1}$), the next question would be how the exchange interaction actually works. Because most of the examples of oxides with DIM are insulating, it becomes clear that the conduction electrons do not play any role in the interaction between the localized moments. In addition, the magnetic dipolar interaction between the localized moments is too weak to produce a magnetic order at RT or above. Therefore, the only possibility that remains is that coupling occurs through the valence band. As we will see in this Review, experimental data indicate that the valence band is spin polarized. In case of ZnO, the spin polarization in the valence band induces a spin polarization in the conduction band (CB) that is retained even above RT.

Is DIM a weak magnetic phenomenon or the contrary? One tends to characterize it as weak simply because the measured ferromagnetic signals are often weak. However, one does not know with certainty the amount of ferromagnetic mass in the sample with defects. Therefore, it is misleading to characterize DIM as a weak phenomenon without knowing the real magnetic mass of the given sample. In the past years, the characterization of the magnetic mass, especially in thin oxide films, got more accurate, and we can nowadays state that the magnetization at saturation reaches $M_s \gtrsim 10\,emug^{-1}$ at 300 K. Does a Curie temperature above 300 K for a defect concentration of $\approx 5\%$ represent a weak magnetic phenomenon? The best way to answer this question is to compare the Curie temperatures triggered by introducing isolated Fe ions in the best matrix Fe can have to trigger magnetic order, which is Pd, a transition metal that almost fulfils the Stoner criterion for magnetic order. Fe ions in Pd get a giant magnetic moment of the order or higher than $10\,\mu_B$. The evolution of Curie temperature with Fe concentration[49] indicates a rather linear dependence, reaching 300 K for Fe concentration of $\approx 15\%$, three times larger than the defect concentration in oxides with DIM. Evidently, DIM cannot be a weak but rather an extraordinarily strong magnetic phenomenon.

This Review has four more sections and a short summary in Section 6. All main theoretical basic concepts, problems to model DIM, origin of the magnetic moments at lattice defects in oxide structures, the transition from localized PM centers to magnetic order through an exchange interaction, and the assistance of the theory to understand experimental results are developed in Section 2. In Section 3, we present and discuss experimental results obtained in ZnO and TiO_2 in the past 11 years. After introducing the reader with a short but important general section on ion irradiation, the next subsections of Section 3 are distributed according to the kinds of samples, such as single

crystals, thin films or microwires, and the experimental evidence obtained from magnetization, X-ray spectroscopy, and magneto-resistance. Section 4 discusses two possible device applications of DIM, such as a spin filter with an extraordinary efficiency and to trigger a robust and large perpendicular magnetic anisotropy (PMA). A short review of the existent literature of DIM in oxides is given in Section 5.

2. Main Principles and Theoretical Results

The basic questions and concepts related to DIM were already addressed in (1)–(6) in Section 1. In this section, the corresponding problems to be solved will be discussed from the theoretical point of view. A detailed study of DIM has to be based on DFT and requires basically a multicode approach, i.e., a series of theoretical methods are necessary to treat the problem. Till now, no theory exists, which describes all aspects of DIM for the manyfold of investigated systems, starting from microscopic properties of defects to ending up with the description of the macroscopic ferromagnetic behavior in a satisfying way.

In Section 2.1, some general concepts will be discussed. Afterward, the single problems mentioned in Section 1 will be considered in some detail. Native defects and their stabilization are in the focus of this consideration. The search of new routes to FM, exploiting native defects in oxides, was encouraged in the work of Elfimov et al.[28] It was shown that divalent cation vacancies within a rocksalt structure, CaO was used as example, lead to a ferromagnetic ground state.

In this section, we restrict to describe the different theoretical methods in their application. We will include references to technical details if necessary.

2.1. General Concepts and Problems to Model DIM

The phenomenon of magnetism in materials can be described by two main approaches. The appearance of band magnetism can be described by the Stoner model. The Stoner criterion is given by $I n^0(E_F) > 1$. Here, $n^0(E_F)$ is the density of states (DOS) of the NM metal at the Fermi energy and I is the exchange integral (Stoner parameter). The DOS of delocalized electrons at the Fermi energy is high if the bandwidth is small. This is realized for 3d bands in, e.g., Fe, and therefore, Fe becomes ferromagnetic.[50]

The other approach is based on local moments. This picture is very successful to explain magnetism in transition metal oxides and fluorides. The magnetic moments are caused by unfilled d or f shells. The magnetism is well described in a Heisenberg model. In transition metal monoxides (TMOs), the antiferromagnetic coupling of the cation moments is described by superexchange via oxygen atoms.[51]

Theoretical work to describe DMSs was for a long time dominated by the discussion of exchange mechanisms that may play a role.[11] If the corresponding exchange constants are known from theory, statistical means can be used to estimate the Curie temperature.[51,52]

Over the years it became clear that defects in the material are more important for the magnetic properties than the transition metal impurities themselves, because the metal impurities have usually a concentration below the percolation threshold. On the one hand, this forces the experimental investigation of DIM in oxides, but on the other hand, it brings more complications to achieve a consistent theoretical description.

Reviews in the literature do not give a final answer about a consistent theory for DIM in oxides. While Zunger et al.[31] pointed out important problems connected with calculations in the framework of DFT, other papers discuss different basic reasons for the appearance of DIM.[5–7,53,54]

There are two ways to develop a consistent picture of DIM. One way is to establish models, which try to catch the main effects by inclusion of a minimum of parameters, if information from experiment is limited. Another way is to start calculations based on DFT for a special suitable system, including as much details as possible.

A model was proposed by Bouzerar and Ziman[55] where a correlated band of oxygen orbitals is used, described with the usual Hubbard Hamiltonian. To describe the cation vacancies of concentration x, a term that is random but locally correlated is added to this Hamiltonian. The Hubbard parameter U, the vacancy potential V_i, and the hole density n_h are the parameters of this minimal model. Disorder is treated exactly by averaging over a large number of states. The electronic structure model calculation is mapped on a Heisenberg model to find the Curie temperature. High Curie temperatures are obtained from the model, but a correlation with experimental data remains difficult.

Magnetism in NM samples might be also achieved by doping with light elements, C in ZnO, for example.[56] If the cation side is doped with an element of smaller valency, calculations in the framework of DFT reveal that the hole doping shifts down the Fermi energy in the p-type valence band. This leads to a spontaneous spin splitting if the Stoner criterion is fulfilled. First-principles calculations for alkali-atom-doped ZrO_2 and TiO_2 proposed such a mechanism.[57,58] Hole doping can be achieved also by cation vacancies, as it was proposed for CaO, ZnO, and other oxides.[28,59] If the substitution takes place at the anion with an atom of smaller valency, shallow spin-polarized gap states are introduced. And if its concentration is high enough, impurity bands form. The band remains spin polarized if the Stoner criterion is fulfilled.

First-principles calculations reveal that native defects in oxides can appear in a high spin state leading to a magnetic moment. The calculated position of the defect level depends on the exchange-correlation functional.[60] The spin state of the defect is connected with the charge state of the defect and therefore with the position of the Fermi level, i.e., with the doping level of the sample. Calculated formation energies give some hints on which defects are the most probable ones in thermodynamic equilibrium under certain growth conditions.[61,62] But theoretical results from bulk calculations might be not easily applied, when defects are created by ion implantation in near surface regions, or if nanostructures, or thin films are used.

Another problem is the correct treatment of disorder. From experiments, very little is known about the exact concentration of the defects and even less about their distribution. The theoretically estimated exchange interaction decreases rapidly with distance. Thus, a low concentration of defects below the magnetic percolation threshold will not lead to FM.[63,64]

Theoretical models are based usually on a homogeneous distribution of defects. In such cases, mean field theories can be applied like coherent potential approximation (CPA) in the framework of the Korringa–Kohn–Rostoker Green's function method (KKR-GF).[65] The method is able to provide exchange parameters but also chemical pair interactions. The chemical pair interaction can be used in principle to create a real space model beyond a random distribution by means of MC simulations, which serves as input to the MC simulation of magnetic properties.[66]

From literature, a lot is known about the single aspects of the problems mentioned earlier. The main unsolved problem is what Zunger et al. called the "burden of proof."[31] Independently of the kind of coupling mechanism between localized moments assumed, one has to prove finally that DIM is stable at RT. The mapping to a Heisenberg model is a consequent route, but it results in too low Curie temperatures.[30] Other theoretical models do not directly calculate Curie temperatures but come to an end when some magnetic entity follows from the calculation. Better results should be found if a closer connection of theory and experiment is achieved with a more precise knowledge on the microscopic structure of the samples.

2.1.1. Problems with Theoretical Framework

The calculation of defect properties has to start with an exact description of the host band structure. For semiconductors and oxides, this is a problem due to pronounced correlation effects.

Drastic examples for this problem are the TMOs, FeO and CoO. Both are metals in the local spin density approximation (LSDA) to DFT but become insulators in agreement with experiments, if correlation corrections are considered.

1) Exchange correlation functional: The results of the fundamental properties of ZnO calculated by different exchange correlation functionals are shown in **Table 1**. The hybrid functionals achieve a sufficient agreement with the experiment, especially for E_g, associated with a high computational effort. The standard general gradient approximation–Perdew–Burke–Ernzernhof (GGA–PBE) formalism underestimates the gap dramatically. This is a major problem because the calculation of defect levels might be tainted with large errors. To get better gap values, the $GGA + U$ formalism[68] is often used as an

alternative with lower computational costs.[30,69–71] A correction of the Zn 3d levels by $U_d \approx 5\,eV$ gives a partial correction and increases the gap to $\approx 1.5\,eV$. A further improvement can be achieved[30,69] with additional corrections to the oxygen 2p orbitals. In multiple scattering approaches, correlation errors are corrected by means of self-interaction corrections.[51,72,73] It has to be noted that a good reproduction of host properties is not a guarantee that defect properties are reproduced properly as well. Calculations for defects in ZnO using the $GGA + U$ formalism[70,74] are often in qualitative agreement with hybrid functional calculations.[60,67,75–77] Thus, important qualitative conclusions can be drawn from $GGA + U$ calculations, but care is necessary to interpret the numerical results.[78] 2) Formation energy: The concentration of the defects that are responsible for DIM is an important quantity. In thermodynamic equilibrium, the concentration c depends on temperature T and the formation energy E^f of the defect by $c = c_0 \exp(-E^f/k_B T)$ (k_B—Boltzmann constant). The concentration c_0 is given by the possibilities to incorporate the defect at different sites of the sample. There exists a well-developed theory to calculate formation energies.[62,79,80] The formation energy E^f for a defect D in charge state q is given by

$$E^f(D, q) = \Delta E_{tot} + \sum n_i \mu_i + q(E_V + \Delta E_F) + E_{corr} \qquad (1)$$

Here, ΔE_{tot} is the difference of the total energies of a supercell of the host material with and without the defect. The chemical potential μ_i of atom sort i is used to consider the change of the number of atoms, if the defect is introduced ($n_i < 0$ if atom is added). E_V is the valence band maximum (VBM) and ΔE_F is the actual position of E_F with respect to VBM. E_{corr} summarizes correction terms. The experimental growth conditions are defined by the choice of the chemical potentials.

As the defects appear in different charge states, the charge-state transition levels $\varepsilon(q + 1/q)$ are also important quantities. The charge-state transition level $\varepsilon(q + 1/q)$ is the position of the Fermi energy in the bandgap, where the formation energies for the charge states $q + 1$ and q are equal. It is obvious from Equation (1) that the accuracy of E^f and $\varepsilon(q + 1/q)$ depends strongly on the quality of the band structure of the host material.

2.2. Origin of Magnetic Moments at Lattice Defects in Oxide Structures

In addition to native defects, a series of NM impurities are discussed as a source of DIM. The discussion here is focused on those defects playing a role in Section 3.

2.2.1. Native Defects in ZnO and Role of H

Native point defects in ZnO are zinc and oxygen vacancies, V_{Zn} and V_O; zinc and oxygen interstitials, Zn_i and O_i; and antisite defects Zn_O and O_{Zn}. Those defects are investigated in a series of papers within the standard DFT framework,[59,81–83] improving the gap by $GGA + U$[30,69,70,74], or by means of hybrid functionals[60,67,71,75–77] (see also the study by Janotti and Van de Walle[78]).
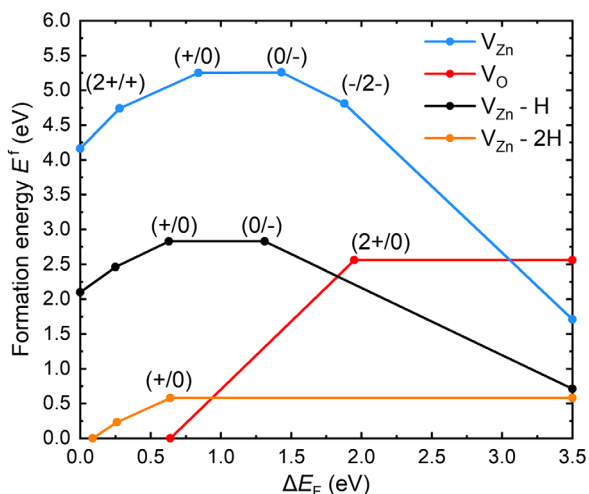
Table 1. Calculated fundamental properties of ZnO for different exchange-correlation functionals. E_d: position of the Zn 3d orbitals, E_g: bandgap, a, c: lattice constants. (Data from ref. [67].) PBE0: hybrid functional Perdew–Burke–Ernzernhof; HSE: hybrid functional Heyd–Scuseria–Ernzernhof; sX: screened exchange.

Functional	a [Å]	c [Å]	E_d [Å]	E_g [Å]
GGA-PBE	3.286	5.299	−4.8	0.74
PBE0	3.257	5.223	−5.9	3.18
HSE ($\alpha = 0.375$)	3.249	5.196	−6.4	3.43
sX[60]	3.267	5.245	−7.0	3.41
Experiment	3.242	5.188	−7.5	3.44

Figure 2. Formation energies E^f and charge-state transition levels $\varepsilon(q+1/q)$ of the native defects and V_{Zn} complexes with hydrogen in ZnO as a function of the position of the Fermi level with respect to the VBM $E_F = E_V + \Delta E_F$. Adapted with permission.[77] Copyright 2017, AIP Publishing.

The calculations agree that oxygen vacancies and zinc vacancies are the defects with lowest E^f. **Figure 2** shows the formation energies for V_{Zn} and V_O and complexes of V_{Zn} with H. For the calculations in Figure 2, the chemical potentials in (1) are chosen to represent an experimental situation in the middle of Zn- and O-rich conditions. The formation energy of V_{Zn} is lower than that of V_O, but it will be further lowered in complexes with hydrogen. The V_{Zn} formation energy becomes even lower for oxygen-rich conditions.

With respect to the experimental part in Section 3, the discussion concentrates on V_{Zn} and its complexes. In a molecular cluster model, four sp^3 molecular orbitals describe the dangling bonds around the Zn vacancy. A single-charged Zn vacancy has an unpaired electron or hole, resulting in a $S = 1/2$ state. For the neutral vacancy, it is found that under T_d symmetry, the hole multiplet splits according to group theory in two irreducible representations, an A_1 singlet and a lower-lying triplet of T_2 symmetry. Two particles in the threefold degenerated T_2 state order the spins parallel in accordance with Hund's rule ($S = 1$). DFT calculations lead to magnetic moments of 1.5 μ_B–2.0 μ_B,[30,59,69,82] depending on the used approximation for the exchange correlation potential.

Calculations using GGA or GGA + U result in a magnetization density distributed on all four neighboring O atoms. It is known experimentally that the two holes are localized on two oxygen p-orbitals only.[84,85] This wrong delocalization does not occur in hybrid function calculations and can also be cured using a GGA+U_{Znd}+U_{Op} scheme, i.e., correlation corrections are applied to the Zn 3d and the O 2p levels.[30] The nonlocal external potential (NLEP) also corrects this spurious delocalization.[86]

Hydrogen is practically unavoidable in any growth process[40,78,87] and further decreases the formation energy of Zn vacancies (cf. Figure 2). Hydrogen at the Zn vacancy forms a bond with one of the neigboring O atoms, reducing the magnetic moment to $\approx$1 μ_B.[30]

2.2.2. Li-Doped ZnO

Lithium is often used as a dopant to produce p-type ZnO.[88] In conjunction with DIM, it has to be analyzed how lithium interstitials Li_i or substitutional lithium Li_{Zn} affect the properties of V_{Zn}, like magnetic moment and formation energy. Defects, like Li_i, Li_{Zn}, Li pairs, and complexes of Li with intrinsic defects are investigated in previous studies.[89–91]

In the studies by Vidya et al. and Nayak et al.,[90,91] Li_i are studied with different exchange correlation functionals. None of the interstitial positions (corresponding to the positions of H[92]) stabilize a magnetic solution. Li_{Zn}^0 results in a polaronic hole localization at one O atom. This is in agreement with a previous theoretical study by Lany and Zunger[86] and experimental data.[93–95] In the study by Nayak et al.,[91] 14 different initial positions of Li_i around V_{Zn} are studied. In a GGA calculation, the ground state is a NM configuration given by the Li interstitial relaxed to the zinc vacancy. More sophisticated functionals result in a magnetic solution of 1 μ_B per supercell.

Calculations of formation energies[89,90,96,97] for different configurations including V_{Zn}, Li_{Zn}, and Li_i reveal a smaller formation energy, especially that of a $V_{Zn} + Li_{Zn} + Li_i$ complex with respect to V_{Zn} alone. A decrease in the formation energy of V_{Zn} will lead to an increase in the defect concentration. Hence, Li is a stabilizer of the magnetic properties of ZnO with V_{Zn}. The theoretical results of Li-doped ZnO can be used to establish a general model for the appearance of magnetism in this material (see Section 3.4).

At low concentrations, Li atoms prefer interstitial sites. An increasing Li concentration leads to a replacement of Zn by Li. These two types of defects do not lead to local magnetic moments. The oxygen partial pressure can be used to choose the oxygen chemical potential such that Li_i+Li_{Zn}+V_{Zn} forms because of a lower formation energy. The complex has a magnetic moment of about 1 μ_B, i.e., lower than V_{Zn} alone. The interstitials Li_i are shallow donors and support n-type ZnO, whereas Li_{Zn} decreases the number of conduction electrons.

2.2.3. Defects in Anatase TiO$_2$

Native defects in rutile TiO$_2$[57,98–106] and anatase TiO$_2$[98,107–116] are investigated theoretically in a number of papers. They follow the line of analysis as discussed for ZnO. Calculations for native defects V_{Ti}, V_O, Ti_i, and O_i[107,109,117,118] demonstrate again the importance of the description of correlation effects.

The calculated formation energies for defects in anatase TiO$_2$ describe a sample in thermodynamic equilibrium. The situation for a comparison of theory and experiments changes, if defects are created by low-energy ion irradiation (see Section 3.1 and 3.5). Simulations of defect formation in such a scenario by means of molecular dynamics methods[121,122] point out that di-Frenkel pairs (di-FPs) are the most important defects in anatase TiO$_2$. GGA + U calculations by means of the Vienna ab initio simulation package (VASP)[123,124] are carried out.[119] If one Frenkel pair is introduced in anatase TiO$_2$, Ti_i migrates back to the vacancy position, ending up in the pristine structure. Two nearest neighbor Frenkel pairs, a di-FP, can be metastable at RT. **Figure 3** shows two di-FP configurations lowest in energy
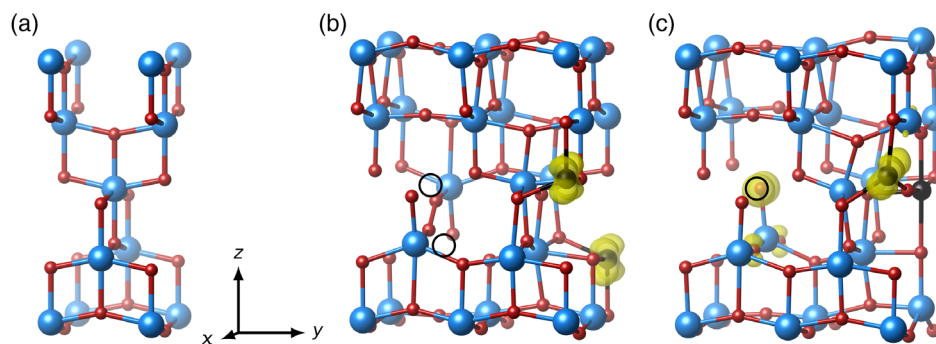
Figure 3. (a) Unit cell of anatase TiO_2 (Ti—blue, O—red), b) di-Frenkel pair type 1 (dFP1), and c) di-Frenkel pair type 2 (dFP2) (Ti vacancies—black circles, Ti interstitials—golden). The spin density is characterized by the yellow isosurfaces. Adapted with permission.[119,120] Copyright 2020, American Physical Society.

carrying a magnetic moment of $2\,\mu_B$ per supercell. In dFP1, shown in Figure 2b, the Ti_i are fivefold coordinated. The magnetic density is mainly located at the interstitial atoms. Only one Ti interstitial is fivefold coordinated in dFP2, as shown in Figure 2c. The spin density is located at one Ti interstitial and oxygen atoms near the vacancies. The structure of the di-FPs found by first-principles calculations serves as the starting point for XMCD calculations (see Section 3.5).

2.3. From Paramagnetism to Magnetic Order

A standard way to discuss the appearance of the ferromagnetic order and calculate the Curie temperature is to map the electronic structure calculation on an effective classical Heisenberg Hamiltonian

$$H = -\sum_{i,j} J_{i,j} e_i \cdot e_j - \sum_i \Delta_i (e_i^z)^2. \tag{2}$$

Here, i and j denote the sites carrying the magnetic moments. $J_{i,j}$ is the exchange coupling constant. The second summand is an anisotropy contribution that plays a role if surfaces or interfaces are considered. Δ_i is the magnetic anisotropy energy (MAE).

The Js in Equation (2) can be calculated by means of the magnetic force theorem (MFT) or from the differences in the total energy of different magnetic structures ED (for details, see the study by Fischer et al.[51]). In "good Heisenberg systems," the interaction is restricted to a few neighbor shells, i.e., only a few Js are sufficient to describe the system. In TMOs, two Js describing the nearest and next-nearest neighbor interaction are used.[51] If the interaction region is more extended, it will be difficult to use the ED approach, and the MFT is preferred. The MAE can be calculated from first principles or considered as an adjustable parameter. Usually the Curie temperature is found by means of MC simulation from Equation (2). A mean field approximation or the random-phase approximation can also be used to estimate the Curie temperature.[51]

2.3.1. Examples

1) That this mapping on a Heisenberg model works for oxides is demonstrated for the series of antiferromagnetic 3d TMO.

The electronic structure is calculated by means of the KKR Green's function method.[65,125] Correlation corrections are implemented by local self-interaction corrections.[72] MFT is used to calculate the exchange parameters for the Heisenberg model in Equation (2). **Table 2** shows the calculated Néel temperatures. In addition to the experimental values, the values calculated by means of the disordered local moment (DLM) method are presented.[126] For individual TMO of the series, more sophisticated investigations can be found in the literature,[127,128] but first-principles calculations predicting the Néel temperatures qualitatively and quantitatively on one level of approximation, as shown in Table 2 for the whole series, are scarce.

2) **Figure 4** shows the exchange coupling constant between two Zn vacancies as a function of their distance in ZnO evaluated from the energy difference of an antiferromagnetic and a ferromagnetic alignment of the moments (ED approach). The obtained values are in agreement with a more recent calculation.[69] Figure 4 shows the result of a GGA + U calculation with corrections applied to the Zn 3d orbitals. The spin density is delocalized on the four O 2p dangling bonds, and the interaction is long ranged. Assuming a concentration of 4.17 at% of vacancies leads to $T_C \approx 60$ K. If the localization of the two holes is forced to be on two oxygen p orbitals by additional correlation corrections to the O p orbitals, the exchange interaction collapses.[30] This problem is basically a percolation problem, i.e., which concentration defines the percolation threshold if the interaction ranges to a certain neighbor shell? The problem was discussed in the studies by Osorio-Guillén et al.[64,110] for HfO_2 and CaO. Considering a short-ranged exchange interaction, the concentration of defects has to be too high to favor high Curie temperatures.

3) The discrepancy between the localization of the two holes on two O p orbitals only and the need for long-range magnetic

Table 2. Néel temperatures calculated with DLM method and MC. (Data from ref. [51]).

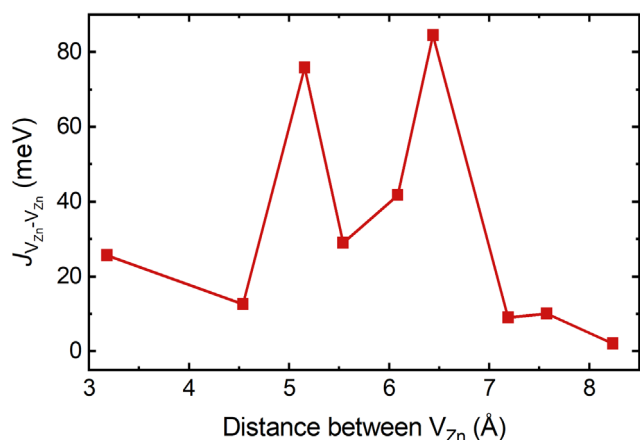| T_N	MnO	FeO	CoO	NiO
Exp.	118	192	289	523
DLM[126]	126	221	242	336
MC	90	162	260	458

Figure 4. Exchange coupling constants of two V_{Zn} as a function of their distance. Adapted with permission.[30] Copyright 2010, IOP Publishing.
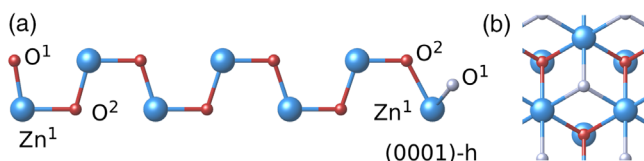

Figure 5. a) Slab unit cell of ZnO after relaxation (blue—Zn, gray, red—O). The $(000\bar{1})$ surface is on the left and the (0001)-h on the RHS. The latter is characterized by the topmost O atom in the threefold coordinated hollow position, O^1, the atoms underneath are labeled Zn^1 and O^2. b) Top view of the (0001)-h surface. Adapted with permission.[73,120] Copyright 2011, American Physical Society.

interaction, as discussed earlier, can be avoided if surfaces or interfaces are considered. FM at the surface becomes more favorable due to lowered symmetry, unsaturated bonds, and uncompensated ionic charges, as demonstrated in the studies by Gallego and coworkers.[129,130] Thus, the ZnO(0001) surface (cf. **Figure 5**) was investigated in a multicode approach. The electronic structure calculation was performed with SIESTA,[131] whereas the magnetic properties are calculated as explained earlier for the TMOs . The layer-resolved density of states (LDOS) shown in **Figure 6**a reflect spin polarization and half metallicity of the surface. The spin-density distribution in Figure 6b shows, as can be deduced also from LDOS, that the main contribution to the total magnetic moment of $\approx 1.5\,\mu_B$ originates from O^1 and O^2. The crystal orbital overlap populations (COOPs) in Figure 6c are a measure of the wave function overlap and therefore a measure of hybridization. Strong hybridization of the atoms near the surface is found.

MC simulations assuming anisotropy parameters of $\Delta_i = 0.1, 0.3, 1.0$, and $3.0\,eV$ lead to critical temperatures of $T_C = 302, 304, 320$, and $346\,K$, i.e., larger than RT, respectively. A more detailed analysis of ZnO surfaces and the role of correlations are presented in the study by Fischer et al.[73] The comparison of bulk and surface calculations points to the fact that DIM at surfaces or in near surface regions is more probable.
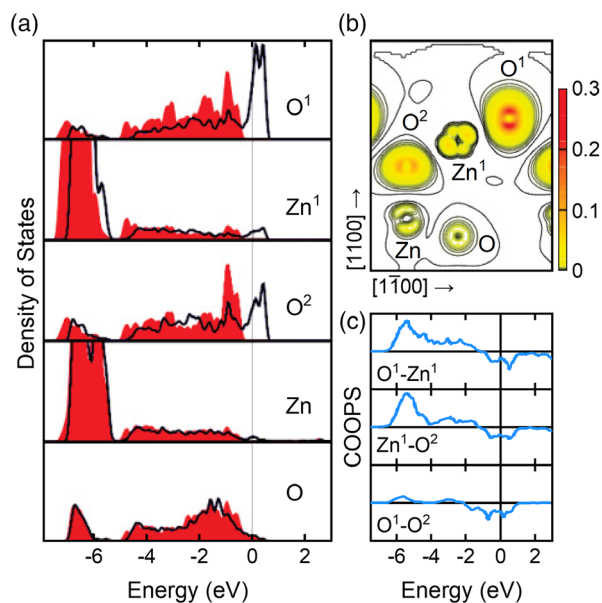

Figure 6. a) Spin-resolved LDOS of the topmost layers of the O-ended (0001)-h crystal structure of ZnO. Red filled (black) values represent majority (minority) spin states. b) Spin density distribution of the (0001)-h surface. c) COOPs between the atoms in the first three layers. Energies are related to E_F. Adapted with permission.[32] Copyright 2011, American Physical Society.

2.3.2. Problems

The discussion on the TMO bulk systems and the ZnO surfaces shares an important feature. The magnetic entities are ordered in a perfect periodic manner. Therefore, no uncertainty with respect to the definition and use of the exchange parameters in the MC calculation exists. Problems occur, as mentioned by Zunger et al.,[31] if DIM has to be investigated like in ZnO with zinc vacancies V_{Zn}. For a corresponding MC run, a random sample with a certain concentration of defects has to be constructed. Hence, the defects occur in a series of different arrangements, whereas the exchange parameters are calculated by means of first-principles methods usually for one fixed arrangement.

The problem of clustering was studied by Hynninen et al.[132] for the FM in (Ga,Mn)N systematically. It was found that randomness reduces the Curie temperatures by 10–20% compared with regular (Ga,Mn)N lattices. In thermal equilibrium, clustering occurs and trimers and tetramers are formed. Increasing clustering reduces T_C strongly. The discussion of clustering in the study by Hynninen et al.[132] considering trimers and tetramers agrees with the results from mean field calculations using the CPA.[133,134] The CPA medium constructed in the studies by Sato et al. and Ebert[133,134] is periodic, i.e., the aforementioned problems do not occur.

2.4. Direct Assistance to Experiments

Finally, it should be mentioned that careful electronic structure calculations can assist experiments in manifold ways without targeting a complete model of DIM. The basic idea is to assume in the electronic structure calculations different defect

configurations to calculate directly experimental quantities. So one can try to figure out indirectly the defect configuration agreeing best with the experiment. For example, an optimization of the lattice structure without and with a certain type and concentration of defects can be directly compared with XRD and positron annihilation data, see Section 3.2.2.

XMCD is an ultimate proof of existing magnetic order in the sample. X-ray absorption spectra can be calculated within different theoretical schemes.[135,136] Results for Li-doped ZnO are presented in Section 3.4. The calculation of the corresponding X-ray absorption spectra and the XMCD is based on a fully relativistic LMTO band structure method.[137] Because the amounts of different defective or pure phases are not known precisely from experiment, a large series of calculations was conducted to fit the spectra. The calculation of the electronic and magnetic properties of vanadium-doped ZnO ($Zn_{1-x} V_x$)O in the study by Bekenov et al.[138] belongs to the same class of problems. The best agreement with experimental XMCD spectra in the study by Ishida et al.[139] is found in this case for two antiferromagnetically coupled vanadium ions with an oxygen vacancy in the first neighbor shell of one of the atoms. The application of X-ray spectroscopy to anatase TiO_2 is discussed in Section 3.5.

Defect engineering, i.e., the creation of special types of defects to achieve or improve the functionality of oxide structures is not restricted to DIM. Oxygen vacancies act as a driving mechanism in the enhancement of the magnetic response of ferrites[140] and are of utmost importance for improving or deteriorating magnetic properties of Sr_2FeMoO_6.[141] Oxides are used in functional units mainly as thin films. Thus, the influence of strain imparted by the substrate to the film due to lattice misfit on defect formation has to be investigated.[142]

3. Experimental Evidence for DIM in ZnO and TiO_2

3.1. Ion Irradiation: A Simple Way to Produce Systematically a Certain Density of Defects and Measure the Magnetic Impurities with High Sensitivity

The irradiation of a sample with energetic ions is an effective and very reproducible way for defect production within the solid. For that purpose, a broad ion beam can be used or a focused ion beam can be scanned across the sample to irradiate it homogeneously or in any dedicated pattern. The ions entering the sample undergo Coulomb interaction with the electrons and nuclei of the host material in a series of binary collisions. As a consequence, the ions lose their energy and come to rest in the material at a depth below the surface, called longitudinal range. This range strongly depends on ion type and energy as well as sample composition and can range from a few nanometers in case of Ar ions with a few hundred electronvolt energy to several tens of micrometers in case of megaelectronvolt protons.

As the ion penetrates the sample, it may transfer an amount of energy to a nucleus in the sample larger than the material-dependent displacement energy, i.e., the energy required to displace the nucleus and with it the atom itself (from the lattice site) and thus produce a point defect. The displaced atom

(recoil atom) as well as the primary ion may have enough energy to displace further atoms from their lattice sites, eventually resulting in a displacement cascade. This process continues until the primary ion as well as all recoil atoms have slowed down to kinetic energies smaller than the displacement energy and finally come to rest.

As for the ion range, the defect density and depth profile also strongly depend on ion type and energy as well as sample composition and can be simulated using the Stopping and Range of Ions in Matter (SRIM) code.[143] It should be noted, however, that SRIM does not consider the defect annealing or the crystalline structure. The defect densities can therefore only be estimated using SRIM with an accuracy that decreases as the ion energy becomes lower. Nevertheless, the defect production using ion irradiation is a reliable and well-reproducible process. Care should be taken with low-energy ion irradiation (< 1 keV) because ion bombardment can not only create the necessary defects for DIM but also can eject particles from the sample's near surface region, i.e., lead to sputtering.[144] In this case, the associated sputtering yield and stoichiometry variations resulting thereof have to be considered for the low-energy irradiation parameters used to avoid the elimination of the near surface magnetic region.

High-energy light ions, e.g., protons or helium ions with $(1 - 3)$ MeV energy, can also be used for the analysis of thin-film composition and thickness using the standard-free methods, Rutherford backscattering spectrometry (RBS)[145] and particle-induced X-ray emission (PIXE).[146] The latter allows for quantitative trace element analysis of impurity atoms, which is of importance to prove further the intrinsic nature of DIM. The minimum detection limits for trace elements strongly depend on the sample properties like film thickness as well as film and substrate composition. For bulk graphite, e.g., minimum detection limits as low as $\approx 50 \, \text{ng} \, \text{g}^{-1}$ have been demonstrated for Fe,[147] significantly superior to energy dispersive X-ray analysis (EDX) or X-ray fluorescence (XRF) commonly used due to the lower bremsstrahlung background. In case of a 100 nm-thick TiO_2 film on $SrTiO_3$, the minimum detection limit for Fe amounts to $\approx 100 \, \mu\text{g} \, \text{g}^{-1}$.

3.2. Magnetization and XRD Results in ZnO Single Crystals and Thin Films

This section is divided into two, considering the kinds of ZnO samples, either single crystals (Section 3.2.1) or thin films (Section 3.2.2).

3.2.1. Single Crystals

Magnetization Measurements after Hydrogen Plasma Treatment: The magnetic properties of hydrothermally grown ZnO single crystals after proton irradiation at low energies ($\simeq 330 \, \text{eV}$) using a H plasma chamber were studied by Khalid et al.[37] The H content after plasma treatment was determined by standard nuclear reaction analysis to be $\approx 2.5 \pm 0.5\%$ within the first $\approx 20 \, \text{nm}$ of the near surface region, after 60 min of treatment at a current of nanoampere through the sample. The 20 nm thickness was estimated using SRIM[143] (see Figure 1 in a previous study[37]).
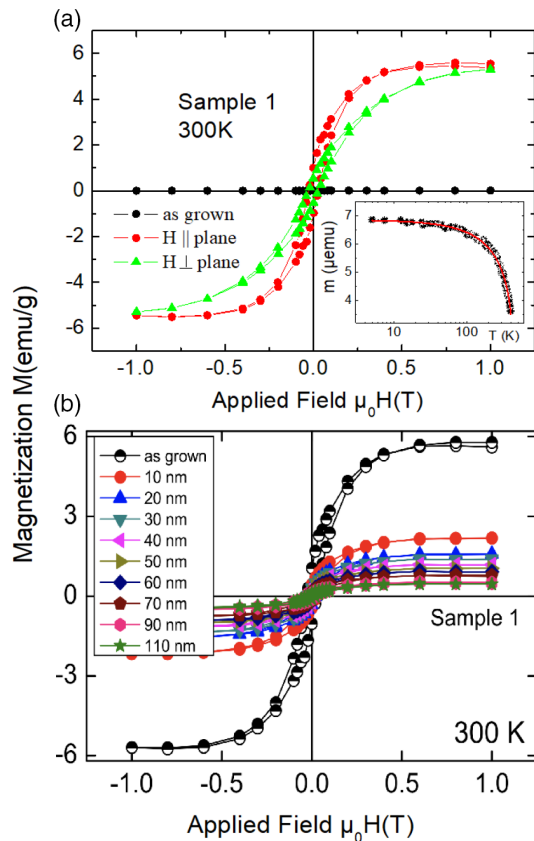
Figure 7. Field magnetization loops at RT of a ZnO single crystal: a) before (black) and after 1 h H plasma treatment at a substrate temperature of 350 °C at two field directions. The inset shows the remanent magnetic moment measured at zero field, after applying a field of 1 T, as a function of temperature. The line through the points is a fit to the function $(1 - (T/T_C))^{1/3}$ with a Curie temperature $T_C = 450$ K. b) Similarly but after removing a certain thickness of the treated surface through chemical etching (field parallel to the main plane). The linear in field diamagnetic background was subtracted from the measured data. Adapted from ref. [37]. Copyright 2011, IOP Publishing Ltd. and Deutsche Physikalische Gesellschaft.

The magnetization results shown in **Figure 7** are obtained for a ZnO crystal treated for 90 min at a substrate temperature of 350 °C. The value of magnetization at saturation at 300 K for this sample was calculated using the measured magnetic moment and assuming a homogeneous magnetic volume of the irradiated area with a 20 nm penetration region. We note that the saturation value of magnetization, at similar H plasma conditions, depends on the substrate temperature reaching a maximum at 350 °C.[37]

The results shown in Figure 7 indicate furthermore the following:

1) The H plasma treatment at the mentioned conditions increased substantially the amount of FM mass in the ZnO-irradiated surface. The ZnO crystal before irradiation did not show a significant FM signal (Figure 7a). There is little doubt on the FM character of the measured field hysteresis. Although there are no measurements of magnetic domains (as for TiO₂, see Section 4.2) or XMCD measurements (as for ZnO:Li microwires, see Section 3.4), the finite hysteresis loop

width indicates a clear remanence. The temperature dependence of the remanence measured at zero field, see inset in Figure 7a, indicates a Curie temperature of $\approx$450 K. 2) The field hysteresis loop shows a clear asymmetry between the field applied parallel or perpendicular to the H plasma-treated crystal plane. Considering the relatively small thickness of the ferromagnetic part at the near surface region of the crystal, the shape anisotropy tends to arrange the magnetization direction parallel to the film plane. From the observed difference between the field loops, one estimates an anisotropy constant, $K_1 \approx 10^5 \mathrm{Jm}^{-3}$. 3) Systematic chemical etching of the surface of the ZnO-treated crystal shows that the magnetization at saturation M_S decreases, see Figure 7b, revealing that a large portion of the FM signal was concentrated in the first 20 nm surface region, as SRIM simulations roughly predicted.[37] Note, however, that about 20% of the maximum magnetization obtained just after H treatment arises from a sample depth nearly six times larger (Figure 7b).

As noted in the study by Khalid et al.,[37] the temperature of the sample during implantation plays an important role in saturation magnetization M_S. This magnetization increases by one order of magnitude between RT and 350 °C sample temperature. As the density of implanted H⁺ in the near surface region would imply having nearly one H⁺ per ZnO unit cell, several orders of magnitude higher than the density of V_O and V_{Zn} created by the implantation,[37] one can estimate an average magnetic moment of 0.2 μ_B per unit cell, comparable with that of H-induced magnetism predicted in the near surface region of ZnO.[33] In contrast, the SRIM MC simulations, used to estimate the density of hydrogen as well as of V_O and V_{Zn}, do not consider the sample temperature. We should also note that the accuracy of the SRIM estimates of the densities (vacancies as well as implanted ions) is doubtful at low ion energies. Obviously, the clear increase in M_S with sample temperature during implantation casts doubts on the significance of the estimated densities obtained with SRIM; we would expect a larger H⁺ diffusion with temperature as well as a decrease in the energy necessary to produce especially V_{Zn}. The results in the study by Khalid et al.,[37] therefore, suggest that not necessarily the H concentration alone is responsible for the observed magnetic order. One possible answer to this dilemma might be related to the implantation of other ions, NM species of a larger mass like Ar⁺, in the H chamber, as studies in TiO₂ films revealed.[148] These higher mass ions may provide the necessary density of V_{Zn} to trigger the magnetic order.

Stability of H⁺ and V_{Zn}: The magnetic order triggered by H plasma treatment was found to be unaffected by aging, maintaining the samples for 1 year at 300 K.[37] This stability may help clarify which main defect is triggering the magnetic order. Regarding the possible diffusion of H⁺ in ZnO, we refer to a recently published work,[149] where Park et al. studied the diffusion properties of H⁺ in ZnO nanorods by nuclear magnetic resonance spectroscopy, before and after 20 MeV proton beam irradiation. They found that the implanted protons occupy thermally unstable sites of ZnO, having an activation barrier of 0.46 eV. Therefore, at 300 K, we would expect clear aging effects within 1 year. What about V_{Zn}? The stability of V_{Zn} produced by (low-energy) irradiation can substantially increase introducing Li impurities (case (b) of Figure 1). Li impurities were found in the measured hydrothermally grown ZnO single crystals by phototoresistance and electron paramagnetic

resonance (EPR) measurements.[150] Because a direct measurement of Li impurities in ZnO is rather difficult, there is no clear value for its concentration in ZnO. We expect that it should be above 100 ppm, at least in some near surface region, as recently published work indicates.[151] The existence of Li impurities in ZnO single crystals has been reported a long time ago.[152] Its influence on the insulating properties of ZnO and the stability effect of V_{Zn} should be always considered, when this vacancy is localized near a Li ion.

Transport Measurements after Hydrogen Plasma Treatment: Magnetotransport measurements are important as a further check for the existence of the magnetic order, specially for the characterization of small samples where the sensitivity of usual magnetometers is insufficient. The other advantage of this characterization is that the magnetotransport is less sensitive to magnetic impurities, if they remain below $\approx 0.1\%$. A possible disadvantage of the magnetotransport characterization is related to the not always simple interpretation of the results, partially due to different scattering contributions of the conduction electrons and/or different conducting paths within the same sample.

Considering the magnetization results of the H plasma-treated ZnO single crystals discussed earlier, it is suitable to discuss now the magnetotransport properties of similar crystals published in the study by Khalid and Esquinazi.[38] **Figure 8** shows the magnetoresistance of three ZnO crystals H1, H2, and H3, at two fixed temperatures, 250 and 10 K. The crystals were implanted with H^+ reaching H concentrations in the first ≈ 20 nm of the order of $\approx 1\%$, $\approx 2\%$, and $\approx 3\%$ (for H1, H2, and H3, respectively), determined by nuclear reaction analysis.
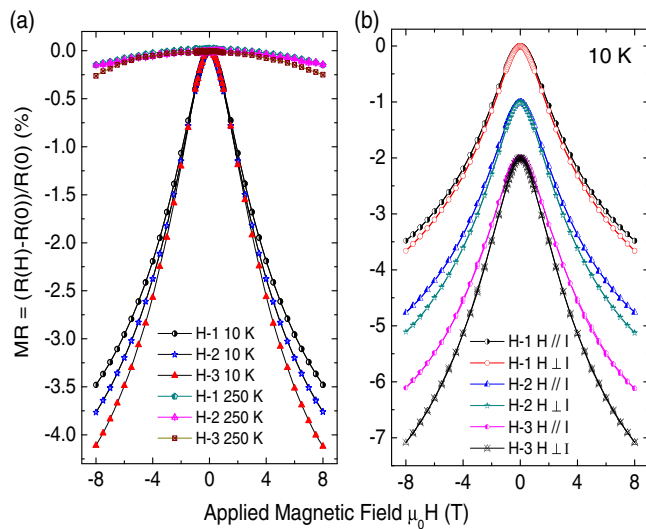

Figure 8. a) Magnetoresistance as a function of the field applied parallel to the magnetic area and to the input current of three H plasma-treated ZnO crystals with H concentration of ≈ 1, ≈ 2, and $\approx 3\%$ (in the first 20 nm of the main surface region) for samples H1, H2, and H3. The magnetoresistance curves are shown at two temperatures, 250 and 10 K. The lines through the points are fits to the semiempirical model of Khosla and Fischer,[153] see Equation (3). b) Field dependence of the magnetoresistance of the samples in (a) but with the field applied parallel and normal to the input current at 10 K, see legend. The curves were shifted in the y-axis for clarity. Adapted with permission.[38] Copyright 2012, American Physical Society.

The electrical contacts were done on the implanted surface. Note that due to the finite penetration depth of H^+ and the inhomogeneous distribution of H within the ≈ 100 nm near surface region, the temperature dependence of the resistance can be understood assuming 1) H-rich metallic regions[154,155] embedded in the semiconducting matrix with an activation energy of ≈ 60 MeV, parallel to 2) the rest of the affected near surface region with a variable range-hopping mechanism.[38] The rest of the ZnO crystal beneath a depth of ≈ 100 nm does not substantially contribute to the measured resistance due to the rather insulating-like properties of (Li-doped) ZnO. Therefore, if one measures transport properties compatible with the existence of the magnetic order, this should be correlated with the near surface sample region as done for the magnetization results.

In general, magnetic materials show a negative magnetoresistance, and this is observed also in H-treated ZnO, as shown in Figure 8a. Its value increases as the temperature decreases and also as the concentration of implanted H^+ increases. The observed behavior shown in Figure 8a can be well understood within a semiempirical model proposed by Khosla and Fischer,[153] where the negative magnetoresistance is attributed to a spin-dependent scattering in the third order of the s–d exchange interaction. The model considers two field-dependent contributions—the positive one with a quadratic field dependence at low fields and a saturation at high fields; first term at the right-hand side (RHS) of Equation (3)

$$\frac{R(H) - R(0)}{R(0)} = c^2 H^2/(1 + (dH)^2) - a^2 \ln(1 + (bH)^2) \quad (3)$$

is due to a Lorentz-force term attributed to two CBs (usually s and d) with different conductivities. The second, negative contribution to the magnetoresistance in Equation (3) is attributed to a spin-dependent scattering between two sub-bands. The coefficients a, b, c, and d are free parameters that depend on the carrier mobility, spin scattering amplitude, exchange integral, and the amplitude of the localized magnetic moments, respectively. For a discussion of these parameters and their relationships to measurable quantities, see the study by Khalid and Esquinazi.[38] Note that a negative magnetoresistance alone does not assure the existence of magnetic order.

Together with magnetization measurements, XMCD results provide a more robust proof. As the XMCD measurements indicate[43] (see Section 3.4), there is a spin-polarized O 2p valence band in ZnO after H plasma treatment. Therefore, it appears plausible that an exchange interaction between 2p electronic states with the Zn d states influences the observed magnetoresistance. We note that within experimental resolution, the magnetoresistance field loop does not show any hysteresis, as in principle, we would expect considering the hysteresis field loops in magnetization (Figure 7). However, considering the coercive fields of the magnetization field loops, the reason is simply the smallness of the hysteresis in the resistance of less than 0.002%, a value clearly below the experimental resolution.

The other fundamental property of magnetically ordered materials is the anisotropy magnetoresistance (AMR). This is measured with the field applied parallel to the input current plane and depends on the angle θ between the current and magnetization vector or applied field direction.[156] AMR is associated

with the spin splitting of the electronic band and a finite spin–orbit coupling. In general, the AMR for fields applied normal to the current direction is (absolutely speaking) larger than for parallel applied fields. This is observed experimentally, as shown in Figure 8b. Moreover, the amplitude of the AMR increases with the H-implanted density, supporting the robustness of the magnetic order state at the implanted surface of the ZnO crystals.

For polycrystalline ferromagnetic samples and in the single domain state (applied field equal or larger than the saturation field), the AMR follows in general a simple angle dependence function $\propto \cos^2(\theta)$. Deviations from this dependence are expected for single ferromagnetic phases when the magnetocrystalline anisotropy plays a significant role. In this case, the angular dependence of the AMR is described by a Fourier series of $\cos(n\theta)$ and $\sin(n\theta)$ with prefactors related to the Hall and magnetoresistance contributions. The experimental results obtained in the study by Khalid and Esquinazi[38] for H-implanted ZnO single crystals not only show a relatively large AMR but also its angle dependence comes from terms with $n = 2, 4, 6$, and 8, indicating also that the Lorentz force on the conduction electrons and holes is not the source of the observed AMR. The temperature dependence of the prefactors of the Fourier series that fits the AMR is not trivial, showing a change of sign at intermediate temperatures in some of the coefficients, similar to the ferromagnetic crystals $U_3 As_4$ and $U_3 P_4$.[157] The origin of the temperature dependence is not yet clarified. In the same publication,[38] the authors demonstrate the existence of an anomalous Hall effect in the same magnetic ZnO crystals with a finite field hysteresis at 300 K.

3.2.2. Thin ZnO Films Produced by PLD in Nitrogen Atmosphere

In the last section, we discussed the magnetic order after H implantation in ZnO crystals. However, good reproducibility and the relatively large H concentration implanted in the near surface region, which are the defects that trigger the observed magnetic order, whether H^+ alone or V_{Zn}–Li–H^+ or other defective structures, could not yet be clearly answered. In this section, we discuss systematic magnetization and XAS measurements obtained on ZnO thin films prepared by PLD in N_2 atmosphere without any doping. The results indicate that V_{Zn} plays a main role in the magnetic order without, however, ruling out the contribution of other defects.

Clearly, the development of magnetic thin films is for possible applications of DMS as well as the DIM phenomenon of high importance. In the case of ZnO, there were many attempts to obtain magnetic thin films at RT, using PLD, radio frequency (RF) magnetron sputtering, or sol–gel method. Even after more than 10 years of experimental research, the necessary details to prepare doped or undoped magnetic ZnO films, whatever the deposition technique, remain still unclear. For example, to cite the most recent studies only (assuming that the observed ferromagnetic response is not due to magnetic impurities), the FM observed in 3% Co-doped ZnO (where Co^{2+} substitutes Zn^{2+}) is strongly enhanced after Ar irradiation,[158] supporting the view that defects play a main role in the observed magnetic order. Without the need of any magnetic ion, RT FM was reported in ZnO:Cu and ZnO:Ag (codoped with Al) thin films prepared by RF sputtering. In contrast, $Zn_{0.95}TM_{0.05}O$ (TM = Co, Ni, Cu) films prepared using a similar deposition technique do not show any magnetic order at RT.[159] These results already suggest that a certain density of defects, like V_O in ZnO:Cu,[46] is necessary to stabilize the magnetic order at RT. In this section, we discuss the magnetic properties of pure ZnO films prepared by PLD at different N_2 partial pressures, where a stable and reproducible RT magnetic order was observed.[160]

After the first hints on the possible influence of certain defects in the observed magnetic order in ZnO films prepared by PLD, reported by Xu et al.,[19] systematic studies of similar films grown at different N_2 pressures on a-, c-, and r-plane $Al_2 O_3$ substrates were published by Khalid et al.[160] A significant ferromagnetic magnetization was obtained only for films deposited on r-plane sapphire substrates, probably due to the nonpolarity of its terminated surfaces, which may facilitate the formation of the necessary defects. The results in **Figure 9**a–d show the following:

a) The lattice constant a of the films decreases for the films prepared with N_2 partial pressures up to 0.3 mbar, remaining nearly constant at higher N_2 pressures.
b) First-principles theoretical results for the ZnO structure with a certain amount of vacancies indicate that the lattice constant a decreases with higher V_{Zn} concentration. This is not obtained for similar amounts of V_O, suggesting the existence of a significant amount of V_{Zn}.
c) The line-shape parameter S obtained from PAS for films prepared at different N_2 partial pressures indicates a clear increase in the amount of vacancies between 0.3 mbar and 0.5 mbar at energies between 2 keV and 4 keV. At these energies the S signals come from the sample surface and interior. At energies $\gtrsim 6$ keV the signal is mainly due to the substrate.
d) The increase in S at intermediate N_2 partial pressures correlates with the clear increase in magnetization at saturation obtained from the field hysteresis loops.

We note that the maximum absolute values of magnetization at saturation of ZnO films are two orders of magnitude smaller than the ones obtained for the H-treated ZnO single crystals; for this compare the results in Figure 7 with those in Figure 9d. On the other hand, it should be clear that such low magnetization values are not compatible to a magnetic order that is stable at 300 K, with further results that suggest a Curie temperature clearly above RT. The reason for these small magnetization values is the division of the measured magnetic moment by the total mass of the ZnO films. In other words, the magnetic signal does not come from all the samples mass but from a small percentage of it. The theoretical calculations indicate a percolation of the magnetic interaction for $\approx 5\%$ of V_{Zn}, which means a magnetization at saturation of $\simeq 7$ emug^{-1}, nearly the values obtained for the H-treated ZnO single crystals and two orders of magnitude larger than the values shown in Figure 9d. These estimates indicate that the order of 1% of the film has the necessary density of defects, e.g., V_{Zn}, to trigger the observed magnetic order. The uncertainty in the magnetic mass or volume of a given sample together with the significant amount of defects, responsible for the observed magnetic signals, is the main open issue in this kind of sample preparation that hinders to some extent a good reproducibility and the comparison among different samples.
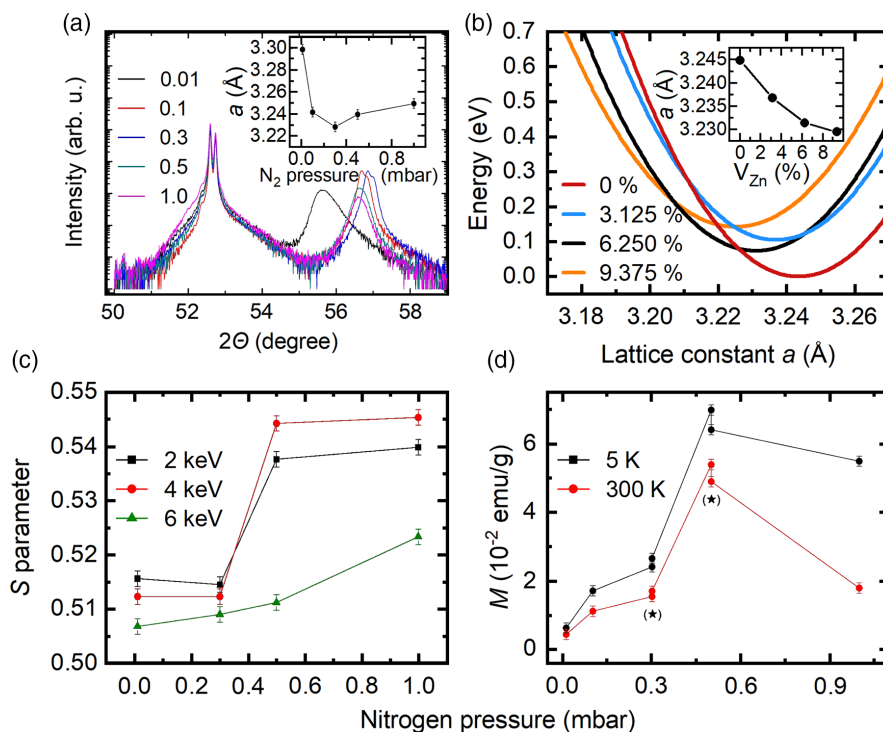
ADVANCED
SCIENCE NEWS
www.advancedsciencenews.com

physica
status
solidi b
www.pss-b.com

Figure 9. a) XRD pattern of ZnO films grown on *r*-plane sapphire substrates at different N_2 partial pressures at a temperature of 400 C by PLD. The inset shows the obtained lattice parameter *a* as a function of N_2 pressure. b) First-principles theoretical calculations of the energy of the system versus the lattice constant *a* of the ZnO lattice with different concentrations of V_{Zn}. The minimum energy indicates the expected lattice constant *a* for different amounts of V_{Zn}, see inset. c) Line-shape parameter *S* obtained from positron annihilation spectroscopy at three different incident positron energies as a function of the N_2 pressure used during film deposition. d) Magnetization at saturation (after subtraction of the diamagnetic background) versus N_2 pressure at 5 K and 300 K. The values marked with (⋆) are from four independently prepared samples. Adapted with permission.[160] Copyright 2009, American Physical Society.

High-resolution XRD and X-ray absorption near-edge structure (XANES) results at the Zn *K*-edge of similar ferromagnetic ZnO thin films together with first-principles calculations using multiple-scattering formalism[161] support the main conclusion of a previous study[160]. We note that XAS provides a powerful tool to investigate defective structures because it probes both the electronic and the structural configuration of specific atoms. **Figure 10**a shows the XANES results for a particular electric field *E* polarization of four ZnO films prepared by PLD at different N_2 partial pressures. One can recognize a clear change of the main central peak, its intensity increases with N_2 partial pressure. Details of the XANES spectra and the changes with N_2 partial pressure depend on the electric field orientation but a qualitative similar result is obtained for $E||(1,0,1)$.

The XRD results indicate a crystallite size of 50(5)nm for all four ZnO films. This known fact in most of the ZnO thin films produced by PLD indicates a substantial amount of grain boundaries. One may speculate that the magnetic order could be related to those boundaries, but there is no evidence for that. Because the crystallite size does not show any significant change with N_2 partial pressure, we can rule out that the crystallite boundaries play an important role in the observed magnetic order. However, they can have a large influence on the electrical transport, reducing substantially the resistivity of the ZnO films in comparison with single-crystalline ZnO samples. For example, in a previous study,[162] the changes of the electrical and optical properties after H plasma

treatment of ZnO thin films prepared by PLD in different atmosphere conditions were studied. The authors conclude that grain boundaries as well as the incorporation of H within them strongly influence the semiconducting properties of ZnO thin films.

To check whether V_O or V_{Zn} is the origin of the observed changes of the main peak with N_2 partial pressures, first-principles calculations of XANES spectra were carried out using clusters of 70–340 atoms.[161] The results of these calculations shown in Figure 10b indicate that only the introduction of V_{Zn} at a certain defined position (named Zn1 in a previous study[161]) but not of V_O produces the increase in the intensity of the main peak in XANES. Moreover, the introduction of V_O in the ZnO cluster gives a strong dependence of the spectra with the polarization of the electric field vector, in disagreement with experimental results. We should note, however, that the first-principle calculations of the XANES spectra were done without taking into account any relaxation of the local structure around the considered vacancy. All the lattice relaxation effects should be examined in future theoretical calculations. For further studies including extended X-ray absorption fine-structure (EXAFS) spectra, see a previous study.[163]

The results shown earlier indicate that V_{Zn} exists in the PLD ZnO films prepared in different N_2 partial pressures and that these vacancies (and not V_O) appear to be of importance to trigger the observed magnetic order. It should be clear that in spite of the use of different characterization techniques, a skeptical reader
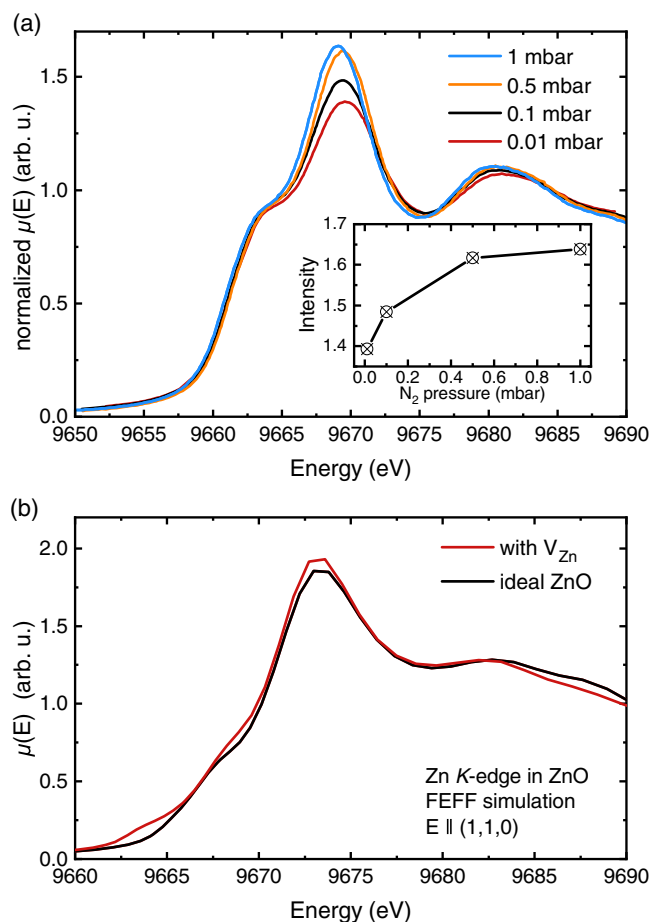
Figure 10. a) XANES spectra of four ZnO thin films prepared by PLD under different N_2 partial pressures (see legend), similar to those, which magnetization is shown in Figure 9d. The thickness of the films were 500, 400, 65, and 60 nm for N_2 partial pressures of 0.01–1 mbar. The measurements were obtained with the electric field of the X-rays parallel to the (1,1,0) direction of the ZnO unit cell in the Cartesian coordinate system. The main peak that changes with the selected N_2 partial pressure (called B in ref. [161]) reflects the summed intensities of electron transitions from Zn 1s → Zn 4p unoccupied states as determined by the orientation of the electric field vector of X-rays in relation to the crystal planes. The inset shows the increase in the intensity of the main peak with N_2 pressure. b) Calculated XANES spectra without (ideal case) and with a density of V_{Zn} of ≃2 at% in the simulated ZnO cluster with 80 atoms. Adapted with permission.[161] Copyright 2011, AIP Publishing.

would not be convinced, taking into account especially that only ≈1% of the total film mass appears to be magnetically ordered. In fact, there are not yet measurements of magnetic domains that may convince the reader of the existence of localized magnetically ordered regions or patches, as is the case of irradiated very thin TiO_2 magnetic layers discussed in Section 3.5 and 4.2. Nevertheless, an important portion of experimental evidence on the intrinsic nature of the defect-induced magnetic order in ZnO and the role of V_{Zn} (see also the discussion in a previous study[29]) is provided by the XMCD measurements on irradiated ZnO microwires, as presented in Section 3.4.

One more open question remains, regarding the observed magnetic order in ZnO PLD films. Why the observed magnetic

order is stable in time? What does pin the responsible V_{Zn} in the atomic lattice at 300 K (or even above)? This stability over time periods of a year or larger may indicate that other defects like foreign ions or more complex defective structures with O, N, or H may exist near V_{Zn}, increasing the pinning potential well for their diffusion to the sample surface.

3.3. ZnO Microwires

In this section we discuss the results of microwires of ZnO. The reason why we have studied these structures, after studying bulk single crystals and thin films, is that the microwires of ZnO have less carriers due to defects, i.e., in general, it means less grain boundaries and therefore more insulating. Thus, their transport properties are much more sensitive to the H^+ implantation than in thin films, for example. Moreover, the relatively large surface/bulk ratio of the microwires enables a more sensitive study of the effects of irradiation and DIM triggered on the near surface region of the wires, see for example a previous study.[164]

3.3.1. Morphology, Tunneling Conductance, and Variable Range-Hopping Mechanisms in the Temperature Dependence of the Resistance

Typical geometry ranges from a few tens of nanometers to several tens of micrometers for diameter and length. The microwires are easily prepared from a high-purity initial material in the form of a powder mixture of ZnO and graphite. The usual carbothermal process involves the thermal decomposition of ZnO at 1150°C in a tubular furnace placed in air.[165] For ZnO microwires of a diameter smaller than ≈1 μm, the perimeter of the wires is rather circular; otherwise, the typical hexagonal shape develops, see **Figure 11**a. The defective structure of the microwire and its influence on the transport depend on the diameter of the wire, as we shall see in this section.

An interesting characteristic of the ZnO microwires is that the main wire axis grows parallel to the c-axis of the wurzite-like structure. Among the possibility to study the transport properties in a different direction as in thin films, it allows also to study the formation of a persistent spin helix at the $(1, 0, \bar{1}, 0)$ surface via the circular photogalvanic effect.[166]

After selecting the microwire from a bundle, it is fixed on a dielectric substrate using amorphous and insulating WC_x,[167] deposited by electron beam induced deposition (EBID), see Figure 11b. For microwires of a small diameter (< 1 μm), the electrical contacts structure is prepared with electron beam lithography and the metallic electrodes are deposited by the sputtering of Cr (5 nm) and Au (35 nm) or Pd/Au contacts, see Figure 11b,c. For microwires of a larger diameter of several micrometers, one can use gold wires clenched with indium on top of the wire. In any case current–voltage ($I - V$) characteristics curves have to be measured to check for nonohmic regimes.

The shape of a ZnO microwire depends on its diameter, if the wire is prepared by the carbothermal process. For diameter below 1 μm, the wires have a circular shape, otherwise hexagonal, see Figure 11. The diameter has also an influence on the internal microstructure and this lasts on the transport properties. In general, the micro- and nanowires of ZnO, at least the ones produced
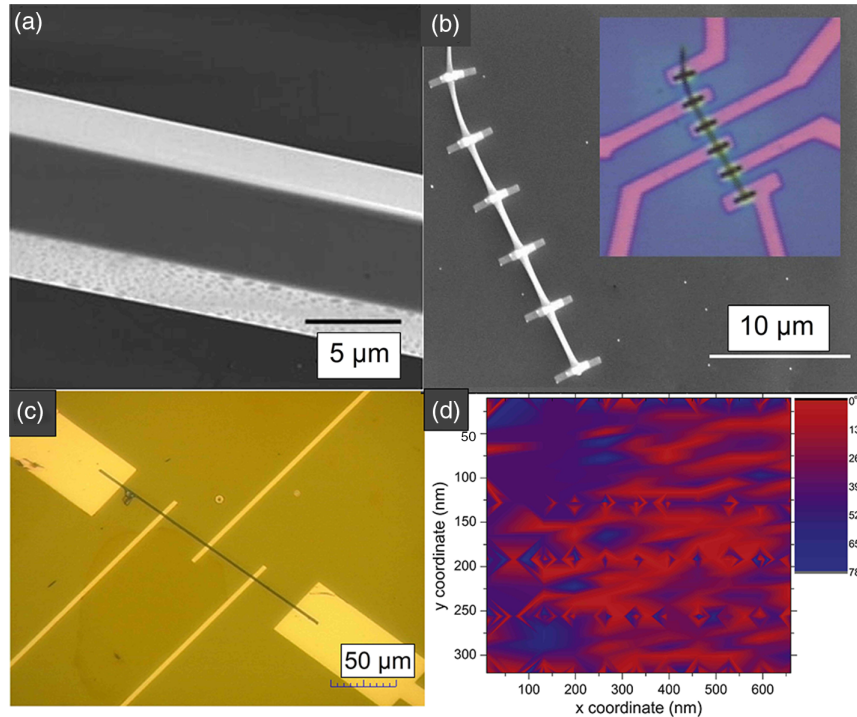
Figure 11. a) Scanning electron microscope (SEM) image of a ZnO microwire with its hexagonal morphology, after H^+ treatment for 1 h at 573 K, Adapted with permission.[168] Copyright 2014, IOP Publishing, b) SEM image of a ZnO microwire of ≈0.4 µm diameter, fixed with EBID-deposited WC_x on a dielectric substrate. The inset shows the microwire with Cr/Au electrical contacts. Adapted with permission.[169] Copyright 2015, IOP Publishing, c) Optical image of a Li-doped ZnO microwire of ≈0.8 µm diameter with five Au contact electrodes prepared to study the electrical noise. Adapted with permission.[170] d) Microstructure of a ≈0.6 µm diameter cylindrical microwire obtained using electron backscatter diffraction (EBSD). The different colors indicate the deviation of the c-axis from the main direction of the microwire, where 0° means the main axis parallel to the (001) direction, and 90° the maximal possible deviation. Adapted with permission.[169] Copyright 2013, Cambridge University Press.

by the carbothermal process, are not really single crystals but are composed of different crystalline regions or a granular-like structure, especially the ones with a small diameter. This can be demonstrated directly by electron backscatter diffraction (EBSD) experiments and indirectly by transport and impedance spectroscopy measurements. Figure 11d shows the deviation of the c-axis from the main direction of a 0.6 µm-diameter wire obtained with EBSD. These results indicate a rather granular-like structure with interfaces between the grains. From these results one can estimate a cross-sectional area ≈ 100 nm × 50 nm for the internal grains,[169] clearly larger than in ZnO thin films produced by PLD.

Current–voltage $(I - V)$ characteristics of a ZnO nanowire are shown in **Figure 12**a, and the temperature dependence of the resistance $R(T, I)$ measured at two constant currents and before and after H^+ irradiation is shown in Figure 12b. The obvious nonlinearities cannot be simply interpreted as due to contact barriers because of the four-point method used[169] but they are related to the granular microstructure of the nanowire. One model that describes the $I - V$ and $R(T, I)$ and takes into account the nonlinear junctions between the grains of the internal microstructure is the fluctuation-induced tunneling conduction (FITC) model.[171] Within this model the electric transport is due to tunneling between large and conducting grains through small contacts, junctions, or thin barriers. The $I - V$ and $R(T, I)$

curves shown in Figure 12a,b can be analyzed assuming that the total current through the sample is given by

$$I_{total} = I_{FITC}(V) + I_a(V) \tag{4}$$

where the first term follows the voltage dependence of the FITC model and the second a linear in voltage term, which comes from the thermally activated semiconducting path. The corresponding parallel resistor sum is

$$R(T)_{total}^{-1} = R_{FITC}(T, I)^{-1} + R_a(T)^{-1} + R_0^{-1} \tag{5}$$

with the first nonohmic term due to the FITC contribution and the second linear term due to the semiconducting path ($\propto \exp(E_a/k_B T)$, with E_a as activation energy), followed by a residual resistance term. This last can be modified after H^+ implantation, see a previous study[169] for more details. The excellent fits to both the $I - V$ curves and the $R(T, I)$ curves minimize the number of free parameters and check the consistency of the free ones.[169] We note that H^+ implantation decreases the resistivity of the ZnO wire by a factor of ten under the used implantation conditions.[169]

A quite different behavior is obtained for ZnO microwires with much larger diameters. Figure 12c shows the temperature dependence of the resistance of three ZnO microwires: an untreated, undoped ZnO, ZH: after H^+ implantation (done
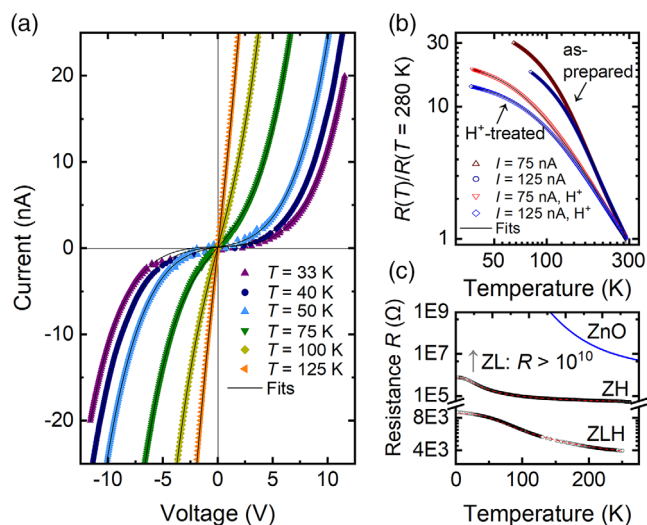
Figure 12. a) Current–Voltage characteristic curves of a $\approx 0.4\,\mu m$ diameter pure ZnO nanowire (see Figure 11b) at different constant temperatures. The curves are linear above 150 K. The lines through the data points are fits to Equation (4), Adapted with permission.[169] Copyright 2015, IOP Publishing, b) Temperature dependence of the resistance measured at two input currents for the nanowire before and after H^+ treatment (1 h at RT and 300 eV energy). The lines through the data points are fits to Equation (5). Adapted with permission.[169] c) Temperature dependence of the resistance of different ZnO microwires with similar diameters of 10 and 300 μm of length. The labels mean: ZnO: pure, untreated ZnO microwire; ZL: (no curve) ZnO with nominally 7% Li; ZH: H^+-implanted ZnO at 373 K for 1 h at 300 eV energy; ZLH: ZnO:Li (7%) after similar H^+ implantation. The dashed red lines through the data points are fits to Equation (6). Adapted with permission.[42] Copyright 2015, IOP Publishing.

1 h at 373 K and 300 eV energy), and ZLH: Li-doped ZnO:Li (7%) after similar H^+ implantation. The resistance at RT of the untreated Li-doped ZnO microwire (ZL) is too large to measure with usual equipments. The measured resistance does not show significant nonlinearities. The temperature dependence of the resistance can be interpreted as due to the parallel contributions

$$R(T)_{\text{total}}^{-1} = R_{\text{VRH}}(T)^{-1} + R_{\text{a}}(T)^{-1} \qquad (6)$$

of a variable range-hopping term $R_{\text{VRH}} \propto \exp\left(E_n/k_B T\right)^p$, with E_n as an effective activation energy and a semiconducting thermally activated term $R_{\text{a}}(T)$.[42] Note a much larger decrease in the resistivity of the undoped ZnO wire in comparison with the one observed in the nanowire in a previous study[169]. This is partially due to the difference in the sample temperature during H^+ implantation, i.e., the higher the sample temperature during implantation, the higher the produced carrier density. This has also a clear influence in magnetoresistance, as we discuss in Section 3.3.2.

Impedance Spectroscopy: An indirect way to obtain information on the conduction mechanisms in granular materials or samples with contributions from internal interfaces is through the measurement of the complex impedance spectroscopy. A plot of the measured reactance versus the resistance, the so-called Cole-Cole plot, of the nanowire of Figure 12a,b indicates that it is composed of three semicircles in the small-diameter microwire.[169]

The three semicircles obtained in this small-diameter microwire can be fitted assuming three resistances and three capacitances in the whole measured range, supporting the idea of different conducting regions or granularity within the microwire.[169] In clear contrast, ZnO microwires of much larger diameters, before or after H^+ implantation at different temperatures, show a single arc in the Cole–Cole plot, indicating a homogeneous single phase or much less granularity than in the smaller-diameter microwires.[168]

3.3.2. Magnetoresistance of H^+-Implanted ZnO Microwires

A way to test the existence of magnetism in a single microwire is through magnetoresistance (MR), as shown for the ZnO bulk single crystals in Section 3.2.1. **Figure 13** shows the field dependence of MR at different constant temperatures of undoped ZnO microwires of larger diameters implanted with H^+ at different temperatures during implantation. As discussed earlier, the density of V_{Zn} produced by H^+ irradiation in pure ZnO without Li doping, remains relatively low because of diffusion. This can be easily recognized in Figure 13a where the MR for a ZnO microwire H^+ treated at 300 K is plotted. The negative MR due to scattering of carriers with localized magnetic moments (see Equation (3)) as well as the overall MR vanishes at $T \gtrsim 50$ K. This indicates a low density of V_{Zn} as well as a low density of carriers produced by H^+ implantation. Increasing the implantation temperature (leaving all other parameters fixed), a positive MR develops, whereas the negative MR remains, contributing below 50 K, see Figure 13b–d. The overall behavior indicates the need to pin enough V_{Zn} produced by H^+ treatment to obtain magnetic order at RT, as observed in the H^+-treated ZnO single crystals. This is achieved by doping ZnO with Li, see Section 3.4.

3.4. ZnO:Li microwires: Magnetization, Magnetoresistance, and XMCD Measurements

3.4.1. Magnetization Measurements

As noted in the case (c) of Section 1, to have a defined density of defects, V_{Zn} in case of pure ZnO, it is necessary to codope ZnO with H and Li, as proposed in the study by Lee and Chang.[44] From one side, H suppresses the formation of compensating interstitials,[172–174] enhancing the acceptor solubility due to the formation of H complexes. In addition, the Li atom is used to pin V_{Zn} nearby, allowing therefore to have a V_{Zn} concentration of the order of the doped Li concentration after ion irradiation. **Figure 14** shows the field hysteresis loops of the magnetic moment measured in three conglomerates of ZnO:Li microwires with different Li concentrations prepared, as described in previous studies.[42,43,165] The results in this figure indicate that a ferromagnetic state at 300 K is triggered after H^+ irradiation only after having a certain density of V_{Zn}, i.e., independently of the irradiated dosis the microwires with only at 1% Li/Zn do not show a ferromagnetic-like field hysteresis loop, compare the results in Figure 14a with those in Figure 14b,c. The estimated concentration of V_{Zn} in the first 10 nm near surface region of the microwires is $3(2) \times V_{\text{Zn}}\,cm^{-3}$, $\approx$ten times the Li concentration
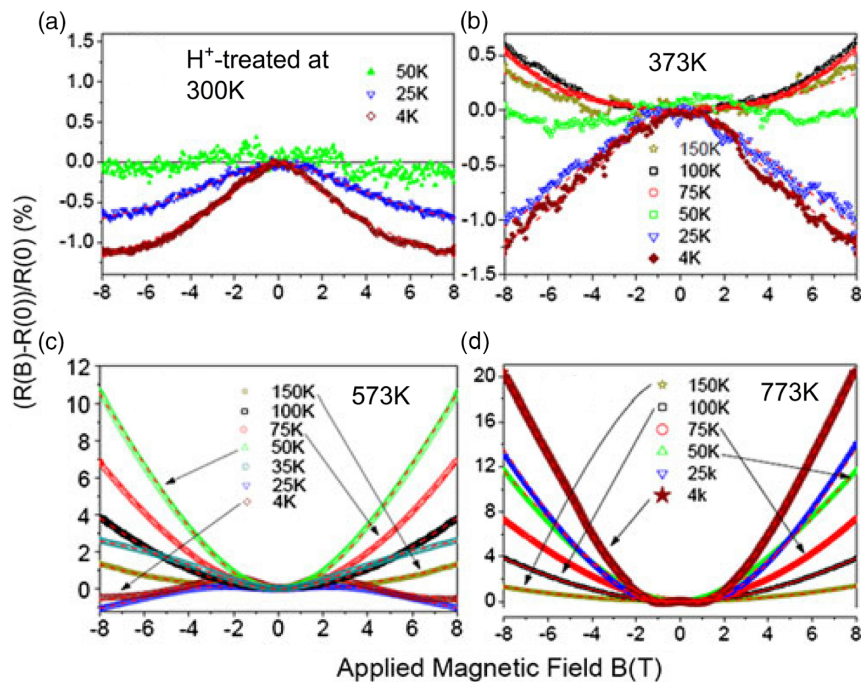
Figure 13. Field dependence of the magnetoresistance of single H$^+$-implanted ZnO microwires of large diameter between 7 and 13 μm at different temperatures. a) Microwire implanted at 300 K, b) at 373 K, c) at 573 K, and d) at 773 K. All wires were H$^+$-implanted 1 h at a constant current of 60 μA. The dashed lines through the data points are fits to Equation (3). Adapted with permission.[168] Copyright 2013, Cambridge University Press.

for the 7 at% Li/Zn sample.[43] We expect, however, that this density of V_{Zn} does not remain constant but most of them diffuse to the surface of the sample, with exception of the ones located near the Li ions, $\approx 3 \times 10^{14}$ (in the first 10 nm of the 7 at% Li/Zn sample).[43]

The results shown in Figure 14 indicate that 1) there is a minimum density of Li doping necessary to trigger FM after H$^+$ irradiation and 2) there is a certain dosis of irradiated H$^+$ necessary to trigger a maximum possible magnetic moment at saturation. Above a certain dosis, the irradiation produces further defects that contribute to a PM response but not a further increase in the ferromagnetic one. Because a direct measurement of the Li concentration in the microwires is difficult, if at all possible due to the light weight of Li ions and because of the relatively small mass of the microwires conglomerates, apart from the magnetization measurements, one needs a further, indirect proof that the nominal Li concentration influences the ZnO lattice. This can be obtained by Raman spectroscopy, where an increase in the nominal Li concentration reduces the Zn-sublattice-related Raman modes systematically.[43] The measured EPR signal also reveals the existence of Li in the microwires, although it is not possible to obtain the absolute concentration from these kinds of measurements.[42]

3.4.2. Magnetoresistance Measurements

As shown in Figure 12c the microwires doped with 7 at%Li/Zn show a large decrease in the electrical resistance after H$^+$ irradiation. As expected and in contrast to the irradiated, undoped ZnO microwires, the Li-doped ZnO microwires show a stable, finite,

and negative MR at all temperatures to 250 K, compare **Figure 15** with Figure 13. The MR data shown in Figure 15 follow very well the semiempirical model described in a previous study[153] and given by Equation (3). A detailed discussion of the obtained fit parameters and the overall temperature dependence of the MR are given in a previous study.[42] The observed field anisotropy shown in Figure 15b indicates that the MR is smaller at fields parallel to the current and main wire c-axis than at normal fields. This result is compatible with the anisotropic MR (AMR) of ferromagnets and similar to that observed in H$^+$-irradiated ZnO crystals, shown in Figure 8b.

We note that the electrical noise represents an important limitation for applications of conducting devices in the nanometer size range and is therefore of interest. The characterization of the intrinsic noise of H$^+$-implanted ZnO:Li microwires at RT was realized.[170] The obtained voltage noise under a constant DC current bias is characterized by $1/f^\alpha$ power spectra (f is the frequency) with $\alpha \sim 1$. The normalized power spectral density tends to be inversely proportional to the carrier density in the probed sample volume.

3.4.3. X-Ray Magnetic Circular Dichroism

We will discuss how XMCD in XAS was used to elucidate the origin of FM in Li-doped ZnO microwires. Before we present the experimental results, we would like to introduce the technique in more detail. XAS and XMCD experiments are commonly conducted at a synchrotron, which is a source of tunable and polarized X-rays with wavelengths between 1 and 100 Å (≈ 10 keV–10 eV). In a XAS experiment, the sample is irradiated

ADVANCED
SCIENCE NEWS
www.advancedsciencenews.com
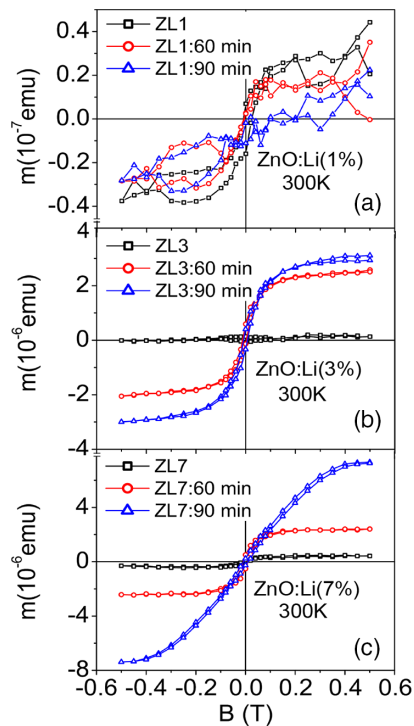
physica
status
solidi b

www.pss-b.com

Figure 14. Magnetic field hysteresis loops of the magnetic moment m obtained at 300 K (after subtraction of a linear diamagnetic background) of ≈ 0.1 cm^2 area conglomerates with different Li concentrations and after different H$^+$ irradiations at 300 eV (see legends): a) 1 at% Li/Zn, b) 3 at% Li/Zn, and c) 7 at% Li/Zn, fixed on a ≈ 0.5 cm^2 conducting substrate area. For example, 1 h at a H$^+$ current of 60 µA implants $\approx 3 \times 10^{18}$ H$^+$ cm^{-2} in the first 10 nm of the microwires. The Li concentrations are nominal values. Adapted with permission.[43] Copyright 2015, AIP Publishing.

Figure 15. Field dependence of the magnetoresistance at different temperatures and field directions with respect to the main wire axis of a 7% Li-doped ZnO microwire (≈ 5 µm diameter) after H$^+$-implantation (1 h with a current of 60 µA at 300 K). a) Magnetoresistance at fields applied always perpendicular to the main wire c-axis. b) Magnetoresistance of the same wire at field applied perpendicular and parallel to the main wire axis at a fixed temperature of 10 K. The continuous lines are fits to Equation (3). Adapted with permission.[42] Copyright 2015, IOP Publishing.

with X-rays of well-defined energy and polarization and the absorption cross section is recorded at each energy by either measuring the intensity of transmitted X-rays (bulk sensitive) or the secondary electron current emitted from a near surface region (≈ 5–10 nm). A certain fraction of X-rays will always be absorbed nonresonantly. However, if the energy of the incident X-ray photon is selected accordingly, the absorption of the X-ray photon will lead to resonant transitions from core-level electrons to empty electronic states above the Fermi level and the occurrence of absorption lines in the spectrum that appear at element-specific characteristic energies. In first order the probability p of this transition can be described by Fermi's golden rule

$$p = |\langle f|\mathbf{D}|i\rangle|^2 \tag{7}$$

where $|i\rangle$ and $\langle f|$ describe the wave function of the initial and final state and $\mathbf{D} = q\mathbf{r}$ represents the Dipole operator. Following dipole transition rules like, e.g., $\Delta \ell = \pm 1$, the excitation of electrons from s orbitals will probe the electronic structure of p states. The exact probability directly depends on the overlap between the wave function of initial and final state and the number of available states (holes) in the final state. It means that XAS is a probe of the local electronic structure.
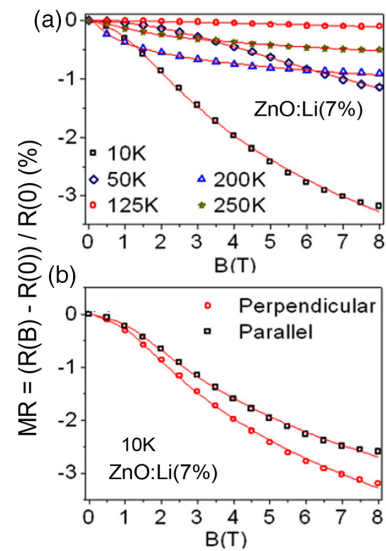
The core-level electron can only be excited—at least with significant probability—into electronic states belonging to the same atomic species and thus the photoexcited electron serves as a direct probe of the unoccupied electronic structure of the atomic species it was excited from. However, as the density and symmetry of the unoccupied states is affected by the local atomic environment, the exact shape of the absorption line is also affected by chemical bonding, charge transfer, etc.

In addition, total angular momentum including the angular momentum of the photon has to be conserved in the XAS process. This causes XAS to be polarization dependent (dichroism) and allows us to detect asymmetries in the final states. One of the most prominent examples is XMCD, where the presence of a spontaneous magnetization caused by spin-polarized electronic states leads to the absence of time-reversal symmetry in the electronic structure. Using circular polarized x-rays, which are not time-reversal invariant (as the helicity of the photon is either parallel or antiparallel to the $\mathbf{k}$-vector), one can now directly probe the existence of spin-polarized electronic states that underlie this missing symmetry in an element-specific quantitative manner. This feature of XMCD has proven immensely useful for the study of DIM, as the element specificity allows to separate parasitic from intrinsic magnetic order. For a more complete review see chapter 9 in a previous study.[175]

We now apply XMCD to elucidate the origin of the magnetic order in H$^+$-implanted ZnO:Li microwires. **Figure 16** shows the XAS spectra (red curves) of two samples labeled ZL1 and ZL3 with 1% and 3% lithium doping, respectively. The difference between these two samples is that ZL3 showed a significant magnetic response after H$^+$ irradiation in contrast to ZL1.[43]
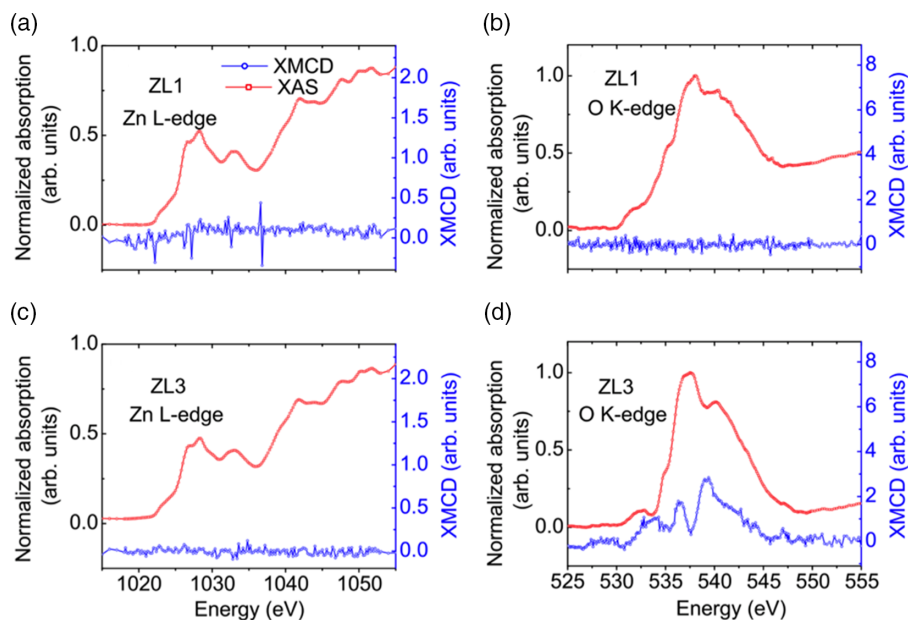
Figure 16. XAS (red) and XMCD (blue) spectra of two H^+-bombarded Li:ZnO samples. a,b) Sample ZL1 was doped with 1% Li and c,d) sample ZL3 with 3% Li. The spectra at the Zn L-edge are shown in the panels (a,c) and those at the O K-edge in (b,d). For comparison in the same figure, the obtained XMCD values were multiplied by $\approx 10^2$. Adapted with permission.[43] Copyright 2015, AIP Publishing.

XMCD spectra were acquired by measuring the XAS yield at each photon energy in alternating applied magnetic fields of ± 0.2 T. Note that this field amplitude is enough to saturate the magnetization of these ferromagnetic wires at 300 K, see Figure 14. The difference of the resulting XAS spectra is the XMCD spectrum, shown in blue in each panel of Figure 16. The first notable observation is that neither sample shows any XMCD difference at the Zn resonance. As the Zn resonance is the result of a 2p–3d dipole transition, it means that the Zn 3d states do not exhibit any magnetic moment or spin polarization. However, we do find that the that oxygen XAS of sample ZL3 shows a distinct XMCD signature, in contrast to sample ZL1, which did not exhibit a macroscopic magnetic signature. Note that the oxygen XAS is caused by electronic 1s–2p transition, meaning one probes the oxygen 2p states in this case. We can therefore conclude that this XMCD signature is directly linked to the magnetism of sample ZL3 and that the magnetic order originates from the oxygen 2p states.

The question now remains if all oxygen atoms contribute to the magnetic order or only at certain atomic lattice sites. One of the strengths of XAS and XMCD is that a variety of simulation packages (band structure or atomic multiplet based) exist, which can be used to model the experimental spectra. In all of the models the simulation parameters can be then linked to directly draw conclusions about the local environment of the investigated atomic species. In this case we used a fully relativistic spin-polarized linear-muffin-tin-orbital method[176,177] and compared the XAS and XMCD spectra to the simulated spectra using perfect ZnO, ZnO with a V_{Zn}, and the ZnO with a V_{Zn} and Li co-doping. As expected, the XAS spectra can be described using a mixture of all of these cases. Remarkably, the XMCD spectrum can be fully described, however, using only ZnO with V_{Zn},

indicating that the origin of the magnetic order in these samples is exactly at those atomic sites, see Figure 4 in a previous study.[43]

Altogether, the combination of an element-specific magnetic probe like XMCD together with meaningful simulations of the obtained spectra provides insight into the electronic states and atomic sites relevant for the observed magnetic order in these H^+-irradiated ZnO:Li microwires. Similarly, in the next section we discuss another example of the application of XMCD in combination with theoretical simulations, where we describe the magnetic order that appears in irradiated anatase TiO_2 samples.

3.5. TiO₂ Anatase Very Thin Magnetic Layers: Magnetization and XMCD Results

Amorphous TiO_2 thin films were prepared by ion-beam sputter deposition with a 1000 eV Xe ion beam sputtering a Ti target. The particles condense on a $LaAlO_3$ (100) substrate, additional O_2 background gas (1.5×10^5 mbar) is provided to obtain the correct stoichiometry. The resulting films have a thickness of about 40 nm, more details are given in the studies by Bundesmann and coworkers.[178,179] After postgrowth annealing at a temperature of $T = 1000$ K for 1 h, epitaxial (001) and polycrystalline anatase thin films were obtained. The samples were then irradiated using Ar^+ ions with an energy of 200 eV and a fluence of 1.0×10^{15} cm^{-2}s^{-1}.

The magnetization measurements were conducted in a standard superconducting quantum interference device (SQUID). In **Figure 17**, the magnetic moment m and magnetization M (right y-axis) as a function of the applied magnetic field $\mu_0 H$ are shown. In case of the as-prepared anatase film, a small initial magnetic moment of ≈ 1 nAm^2 is present. The origin of this
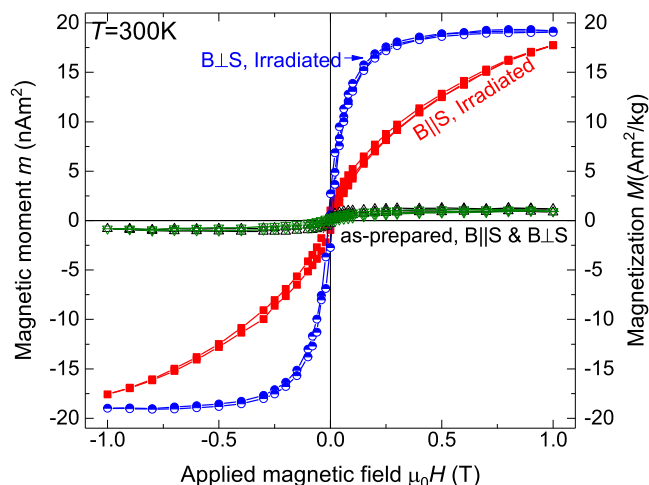
Figure 17. Magnetic moment (left axis) and magnetization (right axis) of the anatase sample before and after irradiation at $T = 300\,K$. The field was applied parallel and perpendicular to the film surface. The magnetization M was calculated assuming a layer thickness of 10 nm. Adapted with permission.[119] Copyright 2020, American Physical Society.

Figure 18. ZFC, FC curves, and remanence of the irradiated anatase thin film. The magnetic field $B = \mu_0 H = 0.05\,T$ was applied perpendicular to the surface (S) of the thin film (ZFC and FC measurements). The temperature sweep direction is indicated by arrows. The remanence was measured at zero applied field after applying a field of 0.05 T. Adapted with permission.[119] Copyright 2020, American Physical Society.

Figure 19. (i) X-ray absorption spectra (top) and magnetic circular dichroism around the Ti-$L_{2,3}$ edges (violet curve) at RT of an irradiated anatase thin film. The applied magnetic fields were $\pm 1\,T$ measured using TEY. The curves (ii)–(v) below show the results of the MultiX XMCD calculations for the two di-FPs and d^0/d^1 ground states. Adapted with permission.[119] Copyright 2020, American Physical Society.

background moment lies in strain-induced magnetism at the LAO/TiO$_2$ interface[180,181] and/or magnetic impurities in the substrate and film.[148]

After irradiation with Ar$^+$ ions, the saturation magnetic moment increases to $\approx 20\,nAm^2$ and a PMA with the easy axis being out of plane, is obtained. Considering the area difference of the two curves measured with the field applied perpendicular and parallel to the surface, one finds an anisotropy constant of $K \approx 0.26\,mJm^{-2}$, similar to the results previously reported for oxides.[182,183] For applications, the thermal stability factor $E/k_B T$ has to be larger than 40[184] to ensure that magnetic information is retained for at least 10 years. With $E = M_{S0} H_K A/2$ being the energy barrier that separates the two magnetization directions, and $K = M_{S0} H_K/2A$, one gets $E/k_B T = KA/k_B T$. Thus, the thermal stability factor is large enough for an area $A \gtrsim 25\,nm^2$. The remanent magnetization (at zero applied field, see **Figure 18**) is rather temperature independent,[148] which rules out superparamagnetism. Consistently, one measures a field hysteresis with a coercive field of $\mu_0 H_c \approx 10\,mT$.

The temperature dependence of the magnetic moment and the remanence of the irradiated sample are shown in Figure 18. The measurement sequence was as usual, i.e., at zero applied field, the temperature was swept from $T = 300\,K$ to $T = 5\,K$; then, a magnetic field of $\mu_0 H = 0.05\,T$ was applied and the heat-up (zero field-cooled [ZFC]) and cool-down (field-cooled [FC]) curves were monitored. As expected for FM, there is an opening between the ZFC and FC curves. Subsequently, the field was turned off and the remanence was measured. The remanent magnetic moment $m(T)$ remains finite at $T \leq 300\,K$; therefore, we expect a Curie temperature well above RT. With the mean field equation $m_{MF}(T) = m_0(1 - T/T_C)^\beta$,[148] we can estimate a Curie temperature of $T_C \approx 550\,K$.

In **Figure 19**, the XAS and the XMDC are shown at the Ti-$L_{2,3}$ edge of the irradiated sample, using total electron yield (TEY). The XAS spectra consist of two edges—the L_3 edge, which
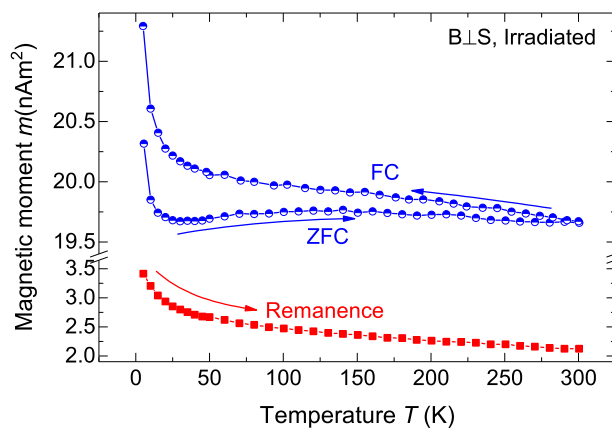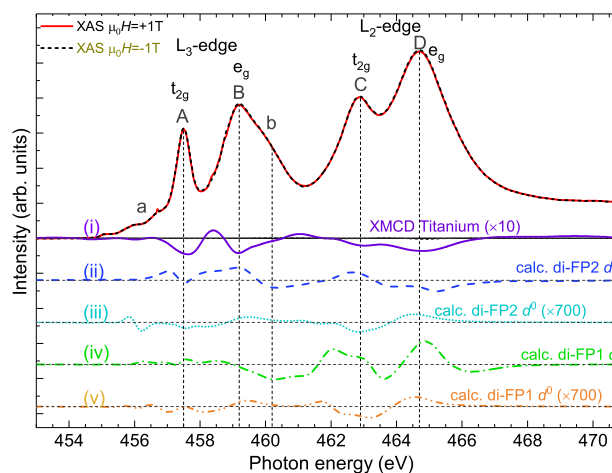
originates from electron transitions from the inner $2p_{3/2}$ orbitals to empty 3d states and the L_2 edge, which is due to $2p_{1/2}$ to 3d transitions. The two edges are split into the four peaks (A–D),[185–188] which are common to all tetravalent Ti compounds with TiO$_6$ coordination[189] and are due to spin–orbit splitting of 2p states (the two L edges) and the 3d splitting to t_{2g} and e_g states. The additional peaks "a" and "b" only appear in case of rutile and anatase.[189–191] The I_B/I_b intensity ratio confirms the anatase phase, where a ratio of $I_B/I_b \geq 1 (I_B/I_b \leq 1)$ corresponds to anatase (rutile). The "b" peak is present, however, much less pronounced compared with the XAS of an untreated sample (**Figure 20**). This confirms that the crystal structure has been modified during irradiation. Further, a finite XMCD signal
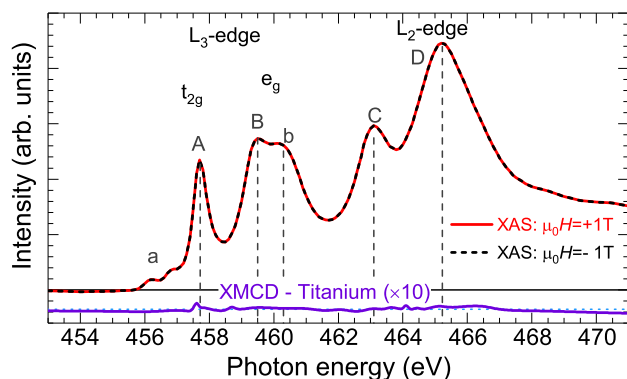
Figure 20. X-ray absorption spectra and magnetic circular dichroism around the Ti-$L_{2,3}$ edges at RT of an untreated sample. The applied magnetic fields were ± 1 T measured using TEY. Adapted with permission.[119] Copyright 2020, American Physical Society.

is obtained (line (i) in Figure 19), which indicates that the Ti atoms have a magnetic moment after irradiation, assuring a magnetically ordered state in the defective TiO_2 oxide structure.

The anatase structures with the di-FP defects were used to calculate the XAS and XMCD spectra,[119] see Figure 19(ii)–(v). The four possible combinations (ground states d^0, d^1, and two different di-FPs) have been shifted for clarity. The best agreement was found for di-FP2 with d^1 ground state, where a Ti dangling bond acts as an O defect, i.e., the formation of TiO_5. None of the calculated XMCD curves agree completely with the experimental data, indicating that other structural changes might be involved in the creation of a magnetic moment in the anatase films. Assuming a defect concentration of one di-FP per two unit cells, and a magnetic moment of $2\,\mu_B$ per di-FP, one finds a defect depth of $\approx$10 nm and a magnetic defect concentration of $\approx$ 8 at%.

In case of the untreated sample, there is no XMCD signal present at RT for the Ti-$L_{2,3}$ edges (Figure 20). This implies that there is no magnetic contribution of Ti at the surface in the nonirradiated anatase films, whereas there is a clear signal for the irradiated sample. The peak energies agree well with literature results.[185,186,189,192,193]

We discuss now the XAS and XMCD results obtained with the luminescence yield (LY). Note that TEY has a probing depth of 5 nm, and it is, therefore, sensitive to surface effects, whereas the LY scans the whole thin film and part of the LaAlO₃ (LAO) substrate. The LY of the Ti-$L_{2,3}$ edges is shown in **Figure 21**. The LY, probing a much larger depth including the substrate/film interface, shows a small XMCD feature, which can explain the initial magnetic moment, which was seen in the SQUID measurements. This can be due to charge transfer at the TiO_2/LAO interface, similar to what has been observed for TiO_2/$SrTiO_3$ interfaces.[194,195] The dotted line in Figure 21 shows the XMCD signal calculated using the code MultiX[196] for anatase in the d^1 ground state, which agrees well with the experimental results. The characteristic XMCD observed before cannot be seen here due to the larger mean free path of the photons compared with the electrons. Furthermore, the b peak intensity confirms that there is a larger contribution of defect-free anatase, compared with the TEY spectrum.
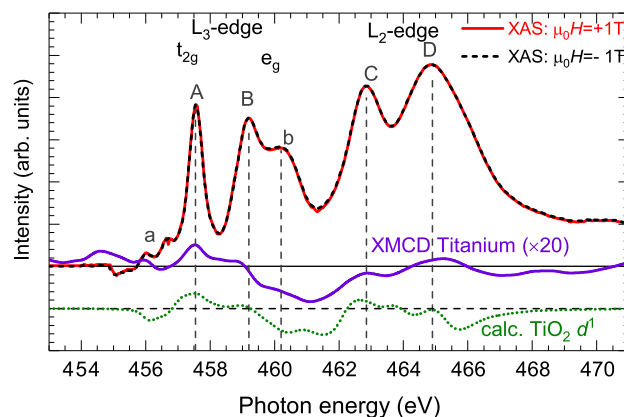

Figure 21. X-ray absorption spectra and magnetic circular dichroism (LY) around the Ti-$L_{2,3}$ edges at RT of an untreated sample. The applied magnetic fields were ± 1 T measured using LY. The dotted lines are the results of the MultiX calculation for anatase with d^1 ground state. Adapted with permission.[119] Copyright 2020, American Physical Society.

4. Examples of Devices for Applications Based on DIM

4.1. Spin Transport and Spin Filtering at Magnetic–Non Magnetic ZnO:Li Homojunctions

As noted in previous sections, experimental data indicate that the valence band in DIM ZnO is spin polarized. A magnetic semiconductor that supports spin-polarized transport is of interest for spintronic applications. We note, however, that the electrical transport in ZnO is mostly n-type due to its tendency to naturally have a surplus of donor defects. In the past decade, huge efforts have been undertaken trying to obtain p-type doping in ZnO but without much success. The difficulty of obtaining p-type ZnO mainly lies in the self-compensation of dopants, i.e., most acceptor dopant elements simultaneously act as donors and therefore, acceptor-doped ZnO is usually insulating. Due to the absence of mobile holes exploiting the spin-polarized valence band in ZnO directly, spin transport appears to be impossible.

As electrical transport is governed by electrons in the CB, we may ask whether it is still possible to obtain a spin-polarized current in ZnO. One way the polarized valence band in ZnO can affect the spin state of free electrons in the CB is by spin-dependent recombination. This effect has been extensively studied in $GaAs_{1-x}N_x$,[197–199] where a certain amount of the Ga ions create PM defect states within the bandgap of $GaAs_{1-x}N_x$. When the PM centers are polarized, either by optical pumping or by applying a magnetic field, the recombination of electrons from the CB through the spin-polarized defects is spin dependent. This results in a dynamic spin polarization of the CB.

The CB of DIM ZnO is also spin polarized, which can be explained by spin-dependent recombination. **Figure 22**a shows the degree of spin polarization $\alpha = (s_\downarrow - s_\uparrow)/(s_\downarrow + s_\uparrow)$ ($s_{\uparrow\downarrow}$ is the majority/minority spin density) of the CB in DIM ZnO:Li as a function of temperature. In contrast to spin-dependent recombination through PM defects, as is the case in $GaAs_{1-x}N_x$, where the PM Ga centers have to be polarized
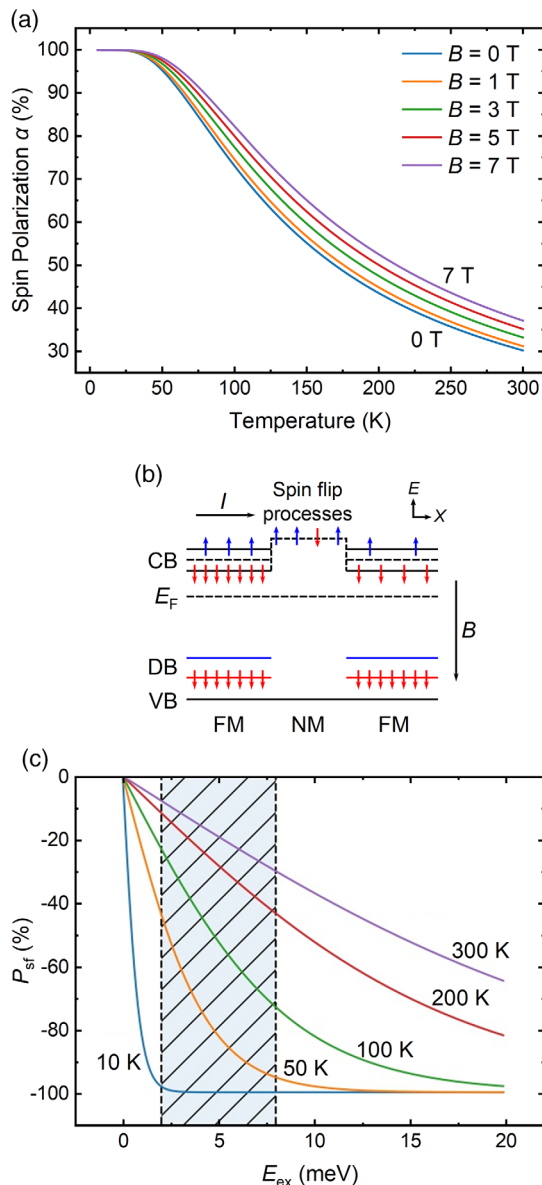
Figure 22. a) Degree of CB spin polarization in DIM Li-doped ZnO. b) Sketch of the energy (E) landscape along a Li:ZnO microwire with highly donor-doped magnetic regions (FM) and less-doped NM regions. The sketch shows the CB minimum, the Fermi level (E_F), the spin-polarized DB within the bandgap and the VBM. The magnetic field direction B is indicated by an arrow. The small blue/red arrows symbolize spin up/down electrons. The rotating arrows in the center symbolize any kind of spin-flip processes. A current I flows from left to right in the x-direction parallel to the c-axis of the ZnO structure and in the sketch normal to the magnetic field direction. The AMR with respect to the angle between field and current is small, see Figure 15b, and for the spin filter effect it can be neglected. c) Spin filter efficiency P_{sf} as a function of the exchange energy E_{ex} at different temperatures in the range 10–300 K and at zero applied magnetic field. The hatched area corresponds to the expected range of E_{ex} in the ZnO:Li spin filter device, with a lower bound of 2 MeV and an upper bound of 8 MeV estimated from magnetoresistance and I–V characteristic measurements. Adapted with permission.[200] Copyright 2019, American Chemical Society.

by external excitation, the spin-dependent recombination in DIM materials works even without external excitation due to the exchange interaction that polarizes spontaneously the valence band.

DIM in ZnO:Li therefore allows to generate spin-polarized currents. As discussed in Section 3.4, DIM can be induced by proton implantation in ZnO:Li microwires, which allows to locally control spin polarization along such a wire by varying the implantation dose. This reminds one of a very common technique used in semiconductor technology to locally control the carrier concentration by varying the amount of doping. In ZnO, Li acts as an acceptor,[201,202] whereas hydrogen acts as a donor dopant. As ZnO:Li is usually insulating, as noted earlier, the proton implantation allows to vary the electron density in the CB within a wide range, before inducing magnetic order.

This ability to locally control the spin polarization and electron concentration along the surface of ZnO:Li samples allows the development of interesting new spintronic devices. For instance, when one implants a high/low dose in alternating regions along a ZnO:Li microwire, such that the highly implanted regions become magnetically ordered and a potential barrier builds between the regions creating magnetic/NM homojunctions, one obtains a minority spin-filter device that inverts spin polarization.[200] Figure 22b shows a sketch of the energy landscape along such a device. In the magnetic regions (FM), the spin-polarized defect band (DB) leads to a spin-polarized CB due to spin-dependent recombinations and to splitting of the spin sub-bands. By changing the electron density in the NM regions, one can tune the height of the potential barrier built at the junction between the regions. Due to the spin splitting of the CB in the FM regions, the potential barrier height is spin dependent. It is higher for majority spins and lower for minority spins. This automatically leads to a filtering of minority spins at the potential barrier and an inversion of spin polarization.

Figure 22c shows the efficiency $P_{sf} = (j_\downarrow - j_\uparrow)/(j_\downarrow + j_\uparrow)$ ($j_{\downarrow\uparrow}$ is the majority/minority spin current density across the spin filter) of this spin filter as a function of the effective magnetic coupling strength E_{ex} in the FM regions. The hatched area shows the range of coupling strength estimated from the I–V characteristic and magnetoresistance measurements.[200] The spin filter efficiency reaches $P_{sf} = 100\%$ at 10 K and $P_{sf} > 10\%$ at RT, an efficiency as good or better than the best spin filters reported in literature.[200]

4.2. PMA in TiO₂ Anatase Microstructures

The results of magnetic force microscopy (MFM) measurements on a patterned anatase film are shown in **Figure 23** for the sample magnetized either antiparallel (Figure 23a) or parallel (Figure 23b) to the magnetization direction of the MFM tip. The pattern has been produced using standard electron beam lithography with PMMA to obtain a mask. After the anatase film was irradiated, the mask was removed completely. Prior to the measurements, the film and the tip were magnetized, as indicated in the figure, and no external field was applied during the measurement.

As expected for a pinned ferromagnetic magnetization vector, the phase shift of the MFM signal depends on the magnetization direction. When changing the relative magnetization direction,
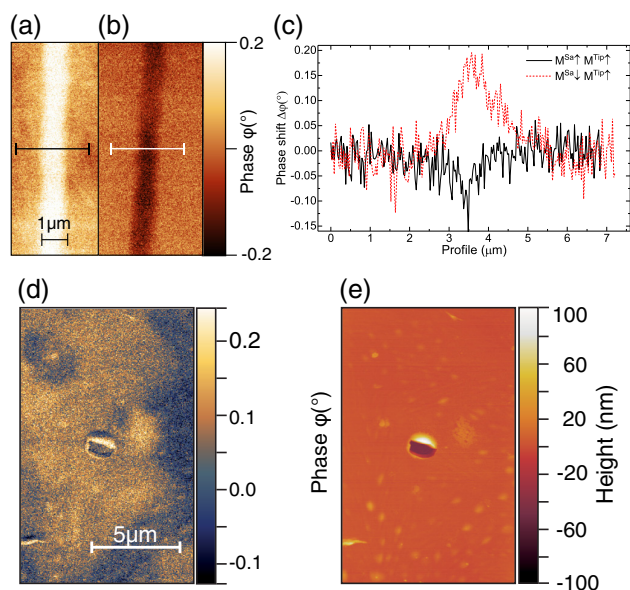
Figure 23. MFM measurements of a magnetically patterned anatase film, with the sample (MS) and tip (MT) magnetization a) antiparallel and b) parallel to each other; c) shows the corresponding line scans. d) An MFM image of an irradiated surface is shown, e) the corresponding topography. Adapted with permission.[119] Copyright 2020, American Physical Society.

a sign change in the phase shift can be observed (see Figure 23c for the linescans indicated in Figure 23a,b). The results clearly indicate that electrostatic influences on the measured MFM phase signal can be ruled out. Furthermore, there is no correlation between phase shift and topography (Figure 23d,e).

The low remanence of the unpatterned and irradiated large-area thin film shown in Figure 18 suggests the existence of randomly ordered domains. Therefore, MFM measurements were conducted on the anatase thin-film surface (Figure 23d). The MFM results indicate the existence of a magnetic domain structure compatible with the low remanence in the SQUID measurements. Furthermore, the measured phase signals confirm that the magnetization direction is pointing out of plane. Note that domains with the magnetization vector in plane would only be recognized at the domain walls, as the out-of-plane field vanishes within the domains. Thus, the MFM results provide an explanation of the magnetic moment measurements and prove that ferromagnetic domains at the surface of the irradiated film exist. These results contradict the theory of paramagnetism due to vacuum fluctuations[203] at least in its current state[53] where a hysteresis/remanence and a magnetic domain structure cannot be explained.

Due to the low magnetic stray fields of the domain structure, the lift scan height was set to −10 nm, and the excitation was reduced such that the tip did not strike the surface. However, surface artifacts cannot be avoided completely (Figure 18d,e), yet the oppositely aligned domains as well as the domain boundaries are not related to topography effects. The magnetic signal remains homogeneous over tens of micrometers, indicating a continuous and smooth distribution of magnetic defects, a clear advantage for applications. Furthermore, the low energy used for irradiation also supports other possibilities for masking

(e.g., with macromolecules[204]) to prepare a magnetic pattern with a very large PMA on the anatase surface.[119]

5. A Short Review on the Existent Literature on DIM in Oxides

As the FM at high temperatures in diluted semiconductors was theoretically predicted, many groups all over the world spent a significant amount of research time within this topic.[205] During the first few years of this research, FM has been unexpectedly observed in many undoped oxides, such as HfO_2,[206–209] CeO_2,[210] TiO_2,[148,209,211,212] In_2O_3,[209,210] ZnO,[160,210,213,214] Al_2O_3,[210] or SnO_2.[207,210,215] Magnetic oxides are not only interesting from the basic physics point of view but also important for applications in a variety of fields, such as magnetic storage,[216] hybrid complementary metal oxide semiconductor or magnetic logic,[182,217] high-frequency components,[218–221] magnetic field sensors,[222] biomedical applications,[223] or giant magnetoresistance sensors.[224,225]

It became evident that doping was not necessary and that magnetism is related to crystal defects. Consequently, it can be accompanied by magnetocrystalline anisotropy. PMA is an important feature for magnetic films due to its application in high-density energy storage, such as magnetic random access memory devices,[183,195,226–230] the enhanced magneto-optical Kerr rotation,[231–233] spin-transfer torque,[194,234] and spin-orbit torque.[235] New magnetic storage devices demand miniaturization, i.e., magnetic bits of the order of 10 nm or less. Materials showing PMA with large anisotropy are of special interest[236] to extend the superparamagnetic limit and obtain higher bit densities.[237]

Magnetic anisotropy can have bulk and/or interfacial contributions originating from spin–orbit interaction, thus inducing a coupling between the magnetization and the crystallographic lattice.[238–240] In multilayers, the origin of the anisotropy varies, e.g., broken symmetry at interfaces,[241,242] the crystallographic mismatch between the layers leading to magnetostriction effects,[243] spin–orbit coupling,[244] or electron hybridization across the interface[245] are possible. This is especially prominent at metal/oxide interfaces, due to hybridization of the metal $3d_{xz}$, $3d_{yz}$, $3d_{z^2}$ orbitals and the oxide 2p orbitals.[246,247] Studies also showed that the interfacial effects are sensitive to their quality,[248] and interfacial anisotropy energies of the order of $\approx 1.5\,mJm^{-2}$, e.g., Co(Fe)(B),[183,249] are typical. Such interfacial PMA is mainly known to occur in bi(tri)-layers made of an oxide and a magnetic layer (and a heavy metal film).[227,242,247,250–255]

In contrast to Co/Pt-based multilayers, heterostructures based on ferromagnet/oxide interfaces[251] exhibit a much lower coercivity, despite PMA. This is advantageous for work based on domain wall propagation, e.g., record domain wall speeds were obtained[256,257] and are, therefore, good candidates for racetrack memories.[258] Current-controlled devices are often limited by their power dissipation; voltage control of magnetism in such systems[256,259–261] could be a way to produce low-power nonvolatile memories and logic devices.

TiO_2 is a good candidate to trigger magnetic order by lattice defects and has been studied in the past,[113,148,192,209,262–264] achieving Curie temperatures to 880 K.[113,212] In general,

magnetism could arise from cation and/or anion defects, and several mechanisms have been proposed for both cases in TiO_2.[113,192,209,212,262–269] For example, studies on HfO_2 or ZrO_2 suggest that the observed FM is due to O vacancies,[206,208,270,271] in disagreement with first-principles theoretical studies, which indicate that O vacancies do not show any magnetic moment in simple, binary oxides but Hf vacancies do.[272] The observed FM in undoped oxide nanoparticles (Al_2O_3, IN_2O_3, ZnO, or SnO_2) was attributed to oxygen vacancies at the surface of the particles.[210] As discussed in previous sections in detail (see Sections 2 and 3.2–3.5), experimental and theoretical studies on the undoped oxide systems of ZnO[19,43,160] indicate that cation vacancies in the bulk of the oxide are indeed responsible for stable magnetic moments and the induced magnetic order[272] when their concentration is around or larger than ≈ 3 at%.[8,43,160]

6. Summary

DIM, sometimes and not always correctly called "d^0-magnetism", is a new phenomenon in solid-state magnetism of unexpected robustness, variability, and complexity. It goes beyond the usual concepts of textbook magnetism with interesting application possibilities in the near future. We should stress that this new kind of magnetic order with extraordinarily high Curie temperatures was born not within the research of oxides (though it may have done this with MgO but scientists did not go further at that time) but in carbon-based samples. Especially, the search for an answer of unclear magnetic signals within the graphite research started much before the diluted semiconductors' short window time. In the cases magnetic impurities were not the answers, defects played the main role in the observed magnetic order.

There are several issues that still remain without satisfactory answers, namely the following. 1) How to produce well-defined amount of defects at specific places of the crystalline lattice? First (but rather brute force) approaches were used with relatively good reproducibility via ion irradiation, annealing at different atmospheres, and mechanical and chemical methods. 2) It is clear that the whole magnetic coupling (we should actually write electric coupling, as magnetism is a phenomenon based on the Coulomb and not magnetic interaction) occurs within the valence band. But do holes or narrow DBs within the energy gap play any role? Or it is simply the overlapping of the binding electronic wave functions at and around the defect that provide the key to understand the DIM phenomenon?

Acknowledgements

Conflict of Interest

The authors declare no conflict of interest.

Keywords

[1] W. Heisenberg, *Z. Phys.* **1928**, *49*, 619.

[2] P. Esquinazi, *Magnetic Carbon, Handbook of Magnetism and Advanced Magnetic Materials* (Eds: H. Kronmüller, S. Parkin), John Wiley & Sohn Ltd, Chichester, UK **2007**, pp. 2256–2281.

[3] Y. Kopelevich, P. Esquinazi, J. Torres, S. Moehlecke, *J. Low Temp. Phys.* **2000**, *119*, 691.

[4] P. Esquinazi, A. Setzer, R. Höhne, C. Semmelhack, Y. Kopelevich, D. Spemann, T. Butz, B. Kohlstrunk, M. Lösche, *Phys. Rev. B* **2002**, *66*, 024429.

[5] O. Volnianska, P. Boguslawski, *J. Phys.: Condens. Matter* **2010**, *22*, 073202.

[6] S. B. Ogale, *Adv. Mater.* **2010**, *22*, 3125.

[7] M. Stoneham, *J. Phys.: Condens. Matter* **2010**, *22*, 074211.

[8] P. Esquinazi, W. Hergert, D. Spemann, A. Setzer, A. Ernst, *IEEE Trans. Magn.* **2013**, *49*, 4668.

[9] *Basic Physics of Functionalized Graphite* (Ed: P. Esquinazi), Springer Series in Materials Science, Vol. *244*, Springer International Publishing AG, Switzerland **2016**.

[10] T. Dietl, H. Ohono, F. Matsukara, J. Cubert, D. Ferrand, *Science* **2000**, *287*, 1019.

[11] K. Sato, L. Bergqvist, J. Kudrnovský, P. H. Dederichs, O. Eriksson, I. Turek, B. Sanyal, G. Bouzerar, H. Katayama-Yoshida, V. A. Dinh, T. Fukushima, H. Kizaki, R. Zeller, *Rev. Mod. Phys.* **2010**, *82*, 1633.

[12] T. Jungwirth, K. Y. Wang, J. Mašek, K. W. Edmonds, J. König, J. Sinova, M. Polini, N. A. Goncharuk, A. H. MacDonald, M. Sawicki, A. W. Rushforth, R. P. Campion, L. X. Zhao, C. T. Foxon, B. L. Gallagher, *Phys. Rev. B* **2005**, *72*, 165204.

[13] J. R. Neal, A. J. Behan, R. M. Ibrahim, H. J. Blythe, M. Ziese, A. M. Fox, G. A. Gehring, *Phys. Rev. Lett.* **2006**, *96*, 197208.

[14] M. Gacic, G. Jakob, C. Herbort, H. Adrian, T. Tietze, S. Brück, E. Goering, *Phys. Rev. B* **2007**, *75*, 205206.

[15] W. Prellier, A. Fouchet, B. Mercey, *J. Phys.: Condens. Matter* **2003**, *15*, R1583.

[16] T. Dietl, H. Ohno, *Rev. Mod. Phys.* **2014**, *86*, 187.

[17] N. H. Hong, N. Poirot, J. Sakai, *Appl. Phys. Lett.* **2006**, *89*, 042503.

[18] Q. Xu, H. Schmidt, L. Hartmann, H. Hochmuth, M. Lorenz, A. Setzer, P. Esquinazi, C. Meinecke, M. Grundmann, *Appl. Phys. Lett.* **2007**, *91*, 092503.

[19] Q. Xu, H. Schmidt, S. Zhou, K. Potzger, M. Helm, H. Hochmuth, M. Lorenz, A. Setzer, P. Esquinazi, C. Meinecke, M. Grundmann, *Appl. Phys. Lett.* **2008**, *92*, 082508.

[20] P. Esquinazi, D. Spemann, R. Höhne, A. Setzer, K. H. Han, T. Butz, *Phys. Rev. Lett.* **2003**, *91*, 227201.

[21] K. H. Han, D. Spemann, P. Esquinazi, R. Höhne, V. Riede, T. Butz, *Adv. Mater.* **2003**, *15*, 1719.

[22] L. Brillson, J. Cox, H. Gao, G. Foster, W. Ruane, A. Jarjour, M. Allen, D. Look, H. von Wenckstern, M. Grundmann, *Materials* **2019**, *12*, 2242.

[23] B. B. Straumal, A. A. Myatiev, P. B. Straumal, A. A. Mazilkin, S. G. Protasova, E. Goering, B. Baretzky, *JETP Lett.* **2010**, *92*, 396.

[24] T. Tietze, P. Audehm, Y. Chen, G. Schütz, B. B. Straumal, S. G. Protasova, A. A. Mazilkin, P. B. Straumal, T. Prokscha, H. Luetkens, Z. Salman, A. Suter, B. Baretzky, K. Fink, W. Wenzel, D. Danilov, E. Goering, *Sci. Rep.* **2015**, *5*, 8871.

[25] M. Ying, A. M. A. Saeedi, M. Yuan, X. Zhang, B. Liao, X. Zhang, Z. Mei, X. Du, S. M. Heald, A. M. Fox, G. A. Gehring, *J. Mater. Chem. C* **2019**, *7*, 1138.

[26] H. Zhang, W. Li, G. Qin, H. Ruan, D. Wang, J. Wang, C. Kong, F. Wu, L. Fang, *Solid State Commun.* **2019**, *292*, 36.

[27] M. D. McCluskey, S. J. Jokela, *J. Appl. Phys.* **2009**, *106*, 071101.

[28] I. S. Elfimov, S. Yunoki, G. A. Sawatzky, *Phys. Rev. Lett.* **2002**, *89*, 216403.

[29] B. Qi, S. Ólafsson, H. Gíslason, *Prog. Mater. Sci.* **2017**, *90*, 45.

[30] W. A. Adeagbo, G. Fischer, A. Ernst, W. Hergert, *J. Phys.: Condens. Matter* **2010**, *22*, 436002.

[31] A. Zunger, S. Lany, H. Raebiger, *Physics* **2010**, *3*, 53.

[32] G. Fischer, N. Sanchez, W. Adeagbo, M. Lüders, Z. Szotek, W. M. Temmerman, A. Ernst, W. Hergert, M. C. Muñoz, *Phys. Rev. B* **2011**, *84*, 205306.

[33] N. Sanchez, S. Gallego, J. Cerdá, M. C. Muñoz, *Phys. Rev. B* **2010**, *81*, 115301.

[34] W. S. Silva, C. Stiehler, E. A. Soares, E. M. Bittar, J. C. Cezar, H. Kuhlenbeck, H. J. Freund, E. Cisternas, F. Stavale, *Phys. Rev. B* **2018**, *98*, 155416.

[35] C. Wang, G. Zhou, J. Li, B. Yan, W. Duan, *Phys. Rev. B* **2008**, *77*, 245303.

[36] C. Woll, *Prog. Surf. Sci.* **2007**, *82*, 55.

[37] M. Khalid, P. Esquinazi, D. Spemann, W. Anwand, G. Brauer, *New J. Phys.* **2011**, *13*, 063017.

[38] M. Khalid, P. Esquinazi, *Phys. Rev. B* **2012**, *85*, 134424.

[39] T. Li, C. S. Ong, T. S. Herng, J. B. Yi, N. N. Bao, J. M. Xue, Y. P. Feng, J. Ding, *Appl. Phys. Lett.* **2011**, *98*, 152505.

[40] C. G. Van de Walle, *Phys. Rev. Lett.* **2000**, *85*, 1012.

[41] X. Xue, L. Liu, Z. Wang, Y. Wu, *J. Appl. Phys.* **2014**, *115*, 033902.

[42] I. Lorite, C. Zandalazini, P. Esquinazi, D. Spemann, S. Friedländer, A. Pöppl, T. Michalsky, M. Grundmann, J. Vogt, J. Meijer, S. P. Heluani, H. Ohldag, W. A. Adeagbo, S. K. Nayak, W. Hergert, A. Ernst, M. Hoffmann, *J. Phys.: Condens. Matter* **2015**, *27*, 256002.

[43] I. Lorite, B. Straube, H. Ohldag, P. Kumar, M. Villafuerte, P. D. Esquinazi, C. E. Rodríguez Torres, S. Perez de Heluani, V. N. Antonov, L. V. Bekenov, A. Ernst, M. Hoffmann, S. K. Nayak, W. A. Adeagbo, G. Fischer, W. Hergert, *Appl. Phys. Lett.* **2015**, *106*, 082406.

[44] E. C. Lee, K. J. Chang, *Phys. Rev. B* **2004**, *70*, 115210.

[45] S. Duhalde, M. F. Vignolo, F. Golmar, C. Chiliotte, C. E. R. Torres, L. A. Errico, A. F. Cabrera, M. Renteria, F. H. Sanchez, M. Weissmann, *Phys. Rev. B* **2005**, *72*, 161313.

[46] T. S. Herng, D. C. Qi, T. Berlijn, J. B. Yi, K. S. Yang, Y. Dai, Y. P. Feng, I. Santoso, C. Sánchez-Hanke, X. Y. Gao, A. T. S. Wee, W. Ku, J. Ding, A. Rusydi, *Phys. Rev. Lett.* **2010**, *105*, 207201.

[47] P. Vachhani, O. Šipr, A. Bhatnagar, R. Ramamoorthy, R. Choudhary, D. Phase, G. Dalba, A. Kuzmin, F. Rocca, *J. Alloys Compd.* **2016**, *678*, 304.

[48] D. C. Agarwal, U. B. Singh, S. Gupta, R. Singhal, P. K. Kulriya, F. Singh, A. Tripathi, J. Singh, U. S. Joshi, D. K. Avasthi, *Sci. Rep.* **2019**, *9*, 6675.

[49] B. H. Yeh, J. Chen, *Chin. J. Phys.* **1975**, *13*, 1.

[50] M. L. Cohen, S. G. Louie, *Fundamentals of Condensed Matter Physics*, Cambridge University Press, Cambridge **2016**.

[51] G. Fischer, M. Däne, A. Ernst, P. Bruno, M. Lüders, Z. Szotek, W. Temmerman, W. Hergert, *Phys. Rev. B* **2009**, *80*, 014408.

[52] S. K. Nayak, M. Ogura, A. Hucht, H. Akai, P. Entel, *J. Phys.: Condens. Matter* **2009**, *21*, 064238.

[53] J. M. D. Coey, *Nat. Mater.* **2019**, *18*, 652.

[54] J. Coey, *Solid State Sci.* **2005**, *7*, 660.

[55] G. Bouzerar, T. Ziman, *Phys. Rev. Lett.* **2006**, *96*, 207602.

[56] H. Pan, J. B. Yi, L. Shen, R. Q. Wu, J. H. Yang, J. Y. Lin, Y. P. Feng, J. Ding, L. H. Van, J. H. Yin, *Phys. Rev. Lett.* **2007**, *99*, 127201.

[57] F. Máca, J. Kudrnovský, V. Drchal, G. Bouzerar, *Appl. Phys. Lett.* **2008**, *92*, 212503.

[58] F. Máca, J. Kudrnovský, V. Drchal, G. Bouzerar, *Philos. Mag.* **2008**, *88*, 2755.

[59] T. Chanier, I. Opahle, M. Sargolzaei, R. Hayn, M. Lannoo, *Phys. Rev. Lett.* **2008**, *100*, 026405.

[60] S. J. Clark, J. Robertson, S. Lany, A. Zunger, *Phys. Rev. B* **2010**, *81*, 115311.

[61] S. K. Nayak, H. T. Langhammer, W. A. Adeagbo, W. Hergert, T. Müller, R. Böttcher, *Phys. Rev. B* **2015**, *91*, 155105.

[62] C. Freysoldt, B. Grabowski, T. Hickel, J. Neugebauer, G. Kresse, A. Janotti, C. G. Van de Walle, *Rev. Mod. Phys.* **2014**, *86*, 253.

[63] J. A. Chan, S. Lany, A. Zunger, *Phys. Rev. Lett.* **2009**, *103*, 16404.

[64] J. Osorio-Guillén, S. Lany, S. V. Barabash, A. Zunger, *Phys. Rev. B* **2007**, *75*, 184421.

[65] A. Ernst, *Multiple-Scattering Theory: New Developments and Applications, Habilitation*, Martin Luther University Halle-Wittenberg **2007**, https://www.osti.gov/etdeweb/servlets/purl/21196671.

[66] B. Sanyal, R. Knut, O. Grnäs, D. M. Iusan, O. Karis, O. Eriksson, *J. Appl. Phys.* **2008**, *103*, 07D131.

[67] F. Oba, A. Togo, I. Tanaka, J. Paier, G. Kresse, *Phys. Rev. B* **2008**, *77*, 245202.

[68] S. L. Dudarev, G. A. Botton, S. Y. Savrasov, C. J. Humphreys, A. P. Sutton, *Phys. Rev. B* **1998**, *57*, 1505.

[69] Q. L. Lin, G. P. Li, N. N. Xu, H. Liu, D. J. E., C. L. Wang, *J. Chem. Phys.* **2019**, *150*, 094704.

[70] A. Janotti, C. G. Van de Walle, *Phys. Rev. B* **2007**, *76*, 165202.

[71] A. Janotti, C. G. Van de Walle, *Phys. Status Solidi B* **2011**, *248*, 799.

[72] M. Lüders, A. Ernst, M. Däne, Z. Szotek, A. Svane, D. Ködderitzsch, W. Hergert, B. L. Györffy, W. M. Temmerman, *Phys. Rev. B* **2005**, *71*, 205109.

[73] G. Fischer, N. Sanchez, W. Adeagbo, Z. Szotek, W. M. Temmerman, A. Ernst, M. Hoffmann, W. Hergert, M. C. Muñoz, *J. Phys.: Condens. Matter* **2016**, *28*, 016003.

[74] A. Janotti, C. G. Van de Walle, *Appl. Phys. Lett.* **2005**, *87*, 122102.

[75] Y. K. Frodason, K. M. Johansen, T. S. Bjørheim, B. G. Svensson, A. Alkauskas, *Phys. Rev. B* **2017**, *95*, 094105.

[76] Y. K. Frodason, K. M. Johansen, T. S. Bjørheim, B. G. Svensson, A. Alkauskas, *Phys. Rev. B* **2018**, *97*, 104109.

[77] J. L. Lyons, J. B. Varley, D. Steiauf, A. Janotti, C. G. Van de Walle, *J. Appl. Phys.* **2017**, *122*, 035704.

[78] A. Janotti, C. G. Van de Walle, *Rep. Prog. Phys.* **2009**, *72*, 126501.

[79] S. B. Zhang, J. E. Northrup, *Phys. Rev. Lett.* **1991**, *67*, 2339.

[80] C. G. Van de Walle, J. Neugebauer, *J. Appl. Phys.* **2004**, *95*, 3851.

[81] Q. Wang, Q. Sun, G. Chen, Y. Kawazoe, P. Jena, *Phys. Rev. B* **2008**, *77*, 205411.

[82] G. Z. Xing, Y. H. Lu, Y. F. Tian, J. B. Yi, C. C. Lim, Y. F. Li, G. P. Li, D. D. Wang, B. Yao, J. Ding, Y. P. Feng, T. Wu, *AIP Adv.* **2011**, *1*, 022152.

[83] D. Kim, J. Yang, J. Hong, *J. Appl. Phys.* **2009**, *106*, 013908.

[84] D. Galland, A. Herve, *Phys. Lett. A* **1970**, *33*, 1.

[85] S. M. Evans, N. C. Giles, L. E. Halliburton, L. A. Kappers, *J. Appl. Phys.* **2008**, *103*, 043710.

[86] S. Lany, A. Zunger, *Phys. Rev. B* **2009**, *80*, 085202.

[87] S. J. Jokela, M. D. McCluskey, *J. Appl. Phys.* **2010**, *107*, 113536.

[88] J. G. Lu, Y. Z. Zhang, Z. Z. Ye, Y. J. Zeng, H. P. He, L. P. Zhu, J. Y. Huang, L. Wang, J. Yuan, B. H. Zhao, X. H. Li, *Appl. Phys. Lett.* **2006**, *89*, 112113.

[89] A. Carvalho, A. Alkauskas, A. Pasquarello, A. K. Tagantsev, N. Setter, *Phys. Rev. B* **2009**, *80*, 195205.

[90] R. Vidya, P. Ravindran, H. Fjellvåg, *J. Appl. Phys.* **2012**, *111*, 123713.

[91] S. K. Nayak, W. A. Adeagbo, H. G. Tran, I. V. Lorite, M. Hoffmann, P. D. Esquinazi, A. Ernst, W. Hergert, The origin of spin polarization in Li doped ZnO from first-principles calculations, unpublished.

[92] S. Limpijumnong, S. B. Zhang, *Appl. Phys. Lett.* **2005**, *86*, 151910.

[93] O. F. Schirmer, *J. Phys.: Condens. Matter* **2006**, *18*, R667.

[94] J. Schneider, O. Schirmer, *Z. Naturforsch. A* **1963**, *18*, 20.

[95] O. Schirmer, *J. Phys. Chem. Solids* **1968**, *29*, 1407.

[96] M. G. Wardle, J. P. Goss, P. R. Briddon, *Phys. Rev. B* **2005**, *71*, 155205.

[97] J. B. Yi, C. C. Lim, G. Z. Xing, H. M. Fan, L. H. Van, S. L. Huang, K. S. Yang, X. L. Huang, X. B. Qin, B. Y. Wang, T. Wu, L. Wang, H. T. Zhang, X. Y. Gao, T. Liu, A. T. S. Wee, Y. P. Feng, J. Ding, *Phys. Rev. Lett.* **2010**, *104*, 137201.

[98] L. B. Shi, Y. P. Wang, *J. Magn. Magn. Mater.* **2016**, *405*, 1.

[99] G. B. Han, S. J. Hu, S. S. Yan, L. M. Mei, *Phys. Status Solidi RRL* **2009**, *3*, 148.

[100] R. Han, H. Yang, D. Wang, X. Du, Y. Yan, *J. Magn. Magn. Mater.* **2015**, *374*, 197.

[101] J. Lu, K. Yang, H. Jin, Y. Dai, B. Huang, *J. Solid State Chem.* **2011**, *184*, 1148.

[102] A. Malashevich, M. Jain, S. G. Louie, *Phys. Rev. B* **2014**, *89*, 075205.

[103] B. J. Morgan, G. W. Watson, *Surf. Sci.* **2007**, *601*, 5034.

[104] Z. Zarhri, M. Houmad, Y. Ziat, O. E. Rhazouani, A. Slassi, A. Benyoussef, A. E. Kenz, *J. Magn. Magn. Mater.* **2016**, *406*, 212.

[105] P. Deák, B. Aradi, T. Frauenheim, *Phys. Rev. B* **2012**, *86*, 195206.

[106] T. He, M. Zhao, L. Mei, *EPL (Europhysics Letters)* **2010**, *90*, 66005.

[107] A. Boonchun, P. Reunchan, N. Umezawa, *Phys. Chem. Chem. Phys.* **2016**, *18*, 30040.

[108] B. J. Morgan, D. O. Scanlon, G. W. Watson, *e-J. Surf. Sci. Nanotechnol.* **2009**, *7*, 389.

[109] B. J. Morgan, G. W. Watson, *J. Phys. Chem. C* **2010**, *114*, 2321.

[110] J. Osorio-Guillén, S. Lany, A. Zunger, *Phys. Rev. Lett.* **2008**, *100*, 036601.

[111] B. Shao, Y. F. He, M. Feng, Y. Lu, X. Zuo, *J. Appl. Phys.* **2014**, *115*, 17A915.

[112] J. Tao, L. Guan, J. Pan, C. Huan, L. Wang, J. Kuo, *Phys. Lett. A* **2010**, *374*, 4451.

[113] S. D. Yoon, Y. Chen, A. Yang, T. L. Goodrich, X. Zuo, K. Ziemer, C. Vittoria, V. G. Harris, *J. Magn. Magn. Mater.* **2007**, *309*, 171.

[114] D. Nechiyil, M. Muruganathan, H. Mizuta, S. Ramaprabhu, *J. Phys. Chem. C* **2017**, *121*, 14359.

[115] Q. Hou, W. Li, C. Li, X. Jia, C. Zhao, *Phys. Lett. A* **2019**, *383*, 186.

[116] H. Peng, J. Li, S. S. Li, J. B. Xia, *Phys. Rev. B* **2009**, *79*, 092411.

[117] S. Na-Phattalung, M. F. Smith, K. Kim, M. H. Du, S. H. Wei, S. B. Zhang, S. Limpijumnong, *Phys. Rev. B* **2006**, *73*, 125205.

[118] B. J. Morgan, G. W. Watson, *Phys. Rev. B* **2009**, *80*, 233102.

[119] M. Stiller, A. T. N'Diaye, H. Ohldag, J. Barzola-Quiquia, P. D. Esquinazi, T. Amelal, C. Bundesmann, D. Spemann, M. Trautmann, A. Chassé, H. B. Hamed, W. A. Adeagbo, W. Hergert, *Phys. Rev. B* **2020**, *101*, 014412.

[120] K. Momma, F. Izumi, *J. Appl. Crystallogr.* **2011**, *44*, 1272.

[121] M. Robinson, N. A. Marks, K. R. Whittle, G. R. Lumpkin, *Phys. Rev. B* **2012**, *85*, 104105.

[122] M. Robinson, N. Marks, G. Lumpkin, *Mater. Chem. Phys.* **2014**, *147*, 311.

[123] G. Kresse, J. Furthmüller, *Phys. Rev. B* **1996**, *54*, 11169.

[124] G. Kresse, J. Furthmüller, *Comput. Mater. Sci.* **1996**, *6*, 15.

[125] M. Lüders, A. Ernst, W. M. Temmerman, Z. Szotek, P. J. Durham, *J. Phys.: Condens. Matter* **2001**, *13*, 8587.

[126] I. D. Hughes, M. Däne, A. Ernst, W. Hergert, M. Lüders, J. B. Staunton, Z. Szotek, W. M. Temmerman, *New J. Phys.* **2008**, *10*, 063010.

[127] W. B. Zhang, Y. L. Hu, K. L. Han, B. Y. Tang, *Phys. Rev. B* **2006**, *74*, 054421.

[128] M. D. Towler, N. L. Allan, N. M. Harrison, V. R. Saunders, W. C. Mackrodt, E. Aprà, *Phys. Rev. B* **1994**, *50*, 5041.

[129] N. Sanchez, S. Gallego, M. C. Muñoz, *Phys. Rev. Lett.* **2008**, *101*, 67206.

[130] S. Gallego, J. I. Beltrán, J. Cerdá, M. C. Muñoz, *J. Phys.: Condens. Matter* **2005**, *17*, L451.

[131] J. M. Soler, E. Artacho, J. D. Gale, A. Garca, J. Junquera, P. Ordejón, D. Sánchez-Portal, *J. Phys.: Condens. Matter* **2002**, *14*, 2745.

[132] T. Hynninen, H. Raebiger, J. von Boehm, *J. Phys.: Condens. Matter* **2006**, *18*, 1561.

[133] L. Bergqvist, O. Eriksson, J. Kudrnovský, V. Drchal, P. Korzhavyi, I. Turek, *Phys. Rev. Lett.* **2004**, *93*, 137202.

[134] K. Sato, W. Schweika, P. H. Dederichs, H. Katayama-Yoshida, *Phys. Rev. B* **2004**, *70*, 201202.

[135] H. Ebert, *Rep. Prog. Phys.* **1996**, *59*, 1665.

[136] J. Rehr, J. Kas, M. Prange, A. Sorini, Y. Takimoto, F. Vila, *C. R. Phys.* **2009**, *10*, 548.

[137] V. V. Nemoshkalenko, A. E. Krasovskii, V. N. Antonov, V. N. Antonov, U. Fleck, H. Wonn, P. Ziesche, *Phys. Status Solidi B* **1983**, *120*, 283.

[138] L. V. Bekenov, V. N. Antonov, S. Ostanin, A. N. Yaresko, I. V. Maznichenko, W. Hergert, I. Mertig, A. Ernst, *Phys. Rev. B* **2011**, *84*, 134421.

[139] Y. Ishida, J. I. Hwang, M. Kobayashi, Y. Takeda, K. Mamiya, J. Okamoto, S. I. Fujimori, T. Okane, K. Terai, Y. Saitoh, Y. Muramatsu, A. Fujimori, A. Tanaka, H. Saeki, T. Kawai, H. Tabata, *Appl. Phys. Lett.* **2007**, *90*, 022510.

[140] C. E. Rodrguez Torres, G. A. Pasquevich, P. M. Zélis, F. Golmar, S. P. Heluani, S. K. Nayak, W. A. Adeagbo, W. Hergert, M. Hoffmann, A. Ernst, P. Esquinazi, S. J. Stewart, *Phys. Rev. B* **2014**, *89*, 104411.

[141] M. Hoffmann, V. N. Antonov, L. V. Bekenov, K. Kokko, W. Hergert, A. Ernst, *J. Phys.: Condens. Matter* **2018**, *30*, 305801.

[142] W. A. Adeagbo, M. Hoffmann, A. Ernst, W. Hergert, M. Saloaro, P. Paturi, K. Kokko, *Phys. Rev. Mater.* **2018**, *2*, 083604.

[143] J. Ziegler, www.srim.org (accessed: 2013).

[144] H. Gnaser, *Interaction of Low-Energy Ions with Solids*, Springer Tracts in Modern Physics, Vol. *146*, Springer Berlin, Heidelberg, New York **1999**, pp. 7–82.

[145] W. Chu, J. Mayer, M. Nicolet, *Backscattering Spectrometry*, Academic Press, New York **1978**.

[146] S. Johansson, J. Campbell, K. Malmqvist, *Particle-Induced X-Ray Emission Spectrometry (PIXE)*, John Wiley & Sons, Inc., New York **1995**.

[147] D. Spemann, P. Esquinazi, A. Setzer, W. Böhlmann, *AIP Adv.* **2014**, *4*, 107142.

[148] M. Stiller, J. Barzola-Quiquia, P. Esquinazi, D. Spemann, J. Meijer, M. Lorenz, M. Grundmann, *AIP Adv.* **2016**, *6*, 125009.

[149] J. K. Park, H. J. Kwon, C. E. Lee, *Sci. Rep.* **2016**, *6*, 23378.

[150] J. Barzola-Quiquia, P. Esquinazi, M. Villafuerte, S. P. Heluani, A. Poppl, K. Eisinger, *J. Appl. Phys.* **2010**, *108*, 073530.

[151] I. Sakaguchi, S. Hishita, *Surf. Interface Anal.* **2004**, *36*, 645.

[152] A. R. Hutson, *Phys. Rev.* **1957**, *108*, 222.

[153] R. Khosla, J. Fischer, *Phys. Rev. B* **1970**, *2*, 4084.

[154] Y. Wang, B. Meyer, X. Yin, M. Kunat, D. Langenberg, F. Traeger, A. Birkner, C. Wöll, *Phys. Rev. Lett.* **2005**, *95*, 266104.

[155] N. Sanchez, S. Gallego, J. Cerdá, M. C. Muñoz, *Phys. Rev. B* **2010**, *81*, 115301.

[156] R. C. O'Handley, *Modern Magnetic Materials*, John Wiley & Sons, New York **2000**.

[157] P. Wiśniewski, *Appl. Phys. Lett.* **2007**, *90*, 192106.

[158] S. Neogi, M. Ahmed, A. Banerjee, S. Bandyopadhyay, *Appl. Surf. Sci.* **2019**, *481*, 443.

[159] P. S. Vachhani, A. H. Rawal, A. K. Bhatnagar, P. Rajput, S. N. Jha, D. Bhattacharyya, *Mater. Res. Express* **2019**, *6*, 066103.

[160] M. Khalid, M. Ziese, A. Setzer, P. Esquinazi, M. Lorenz, H. Hochmuth, M. Grundmann, D. Spemann, T. Butz, G. Brauer, W. Anwand, G. Fischer, W. A. Adeagbo, W. Hergert, A. Ernst, *Phys. Rev. B* **2009**, *80*, 035331.

[161] J. Haug, A. Chassé, M. Dubiel, C. Eisenschmidt, M. Khalid, P. Esquinazi, *J. Appl. Phys.* **2011**, *110*, 063507.

[162] I. Lorite, J. Wasik, T. Michalsky, R. Schmidt-Grund, P. Esquinazi, *Thin Solid Films* **2014**, *556*, 18.

[163] J. Timoshenko, A. Anspoks, A. Kalinko, A. Kuzmin, *Acta Mater.* **2014**, *79*, 194.

[164] I. Lorite, Y. Kumar, P. Esquinazi, C. Zandalazini, S. P. de Heluani, *Small* **2015**, *11*, 4403.

[165] M. Villafuerte, J. M. Ferreyra, C. Zapata, J. Barzola-Quiquia, F. Iikawa, P. Esquinazi, S. P. Heluani, M. M. de Lima, A. Cantarero, *J. Appl. Phys.* **2014**, *115*, 133101.

[166] L. Botsch, I. Lorite, Y. Kumar, P. Esquinazi, *Phys. Rev. B* **2017**, *95*, 201405.

[167] D. Spoddig, K. Schindler, P. Rödiger, J. Barzola-Quiquia, K. Fritsch, H. Mulders, P. Esquinazi, *Nanotechnology* **2007**, *18*, 495202.

[168] I. Lorite, P. Esquinazi, C. Zapata, S. P. Heluani, *J. Mater. Res.* **2014**, *29*, 78.

[169] M. Stiller, J. Barzola-Quiquia, M. Zoraghi, P. Esquinazi, *Nanotechnology* **2015**, *26*, 395703.

[170] B. Dolgin, I. Lorite, Y. Kumar, P. Esquinazi, G. Jung, B. Straube, S. P. de Heluani, *Nanotechnology* **2016**, *27*, 305702.

[171] P. Sheng, *Phys. Rev. B* **1980**, *21*, 2180.

[172] A. Zunger, *Appl. Phys. Lett.* **2003**, *83*, 57.

[173] C. H. Park, S. B. Zhang, S. H. Wei, *Phys. Rev. B* **2002**, *66*, 073202.

[174] R. Y. Tian, Y. J. Zhao, *J. Appl. Phys.* **2009**, *106*, 043707.

[175] J. Stöhr, H. C. Siegmann, *Magnetism – From Fundamentals to Nanoscale Dynamics*, Springer Series in Solid State Sciences, Vol. 152, Springer Heidelberg **2006**.

[176] O. K. Andersen, *Phys. Rev. B* **1975**, *12*, 3060.

[177] V. V. Nemoshkalenko, A. E. Krasovskii, V. N. Antonov, V. N. Antonov, U. Fleck, H. Wonn, P. Ziesche, *Phys. Status Solidi B* **1983**, *120*, 283.

[178] C. Bundesmann, H. Neumann, *J. Appl. Phys.* **2018**, *124*, 231102.

[179] C. Bundesmann, T. Lautenschläger, D. Spemann, A. Finzel, E. Thelander, M. Mensing, F. Frost, *Appl. Surf. Sci.* **2017**, *421*, 331.

[180] J. S. Lee, Y. W. Xie, H. K. Sato, C. Bell, Y. Hikita, H. Y. Hwang, C. C. Kao, *Nat. Mater.* **2013**, *12*, 703.

[181] H. Y. Hwang, Y. Iwasa, M. Kawasaki, B. Keimer, N. Nagaosa, Y. Tokura, *Nat. Mater.* **2012**, *11*, 103.

[182] B. Dieny, R. Sousa, J. Herault, C. Papusoi, G. Prenat, U. Ebels, D. Houssameddine, B. Rodmacq, S. Auffret, L. B. Prejbeanu, M. Cyrille, B. Delaet, O. Redon, C. Ducruet, J. P. Nozieres, I. Prejbeanu, *Int. J. Nanotechnol.* **2010**, *7*, 591.

[183] S. Ikeda, K. Miura, H. Yamamoto, K. Mizunuma, H. D. Gan, M. Endo, S. Kanai, J. Hayakawa, F. Matsukura, H. Ohno, *Nat. Mater.* **2010**, *9*, 721.

[184] S. Ikeda, J. Hayakawa, Y. M. Lee, F. Matsukura, Y. Ohno, T. Hanyu, H. Ohno, *IEEE Trans. Electron Devices* **2007**, *54*, 991.

[185] E. Stoyanov, F. Langenhorst, G. Steinle-Neumann, *Am. Mineral.* **2007**, *92*, 577.

[186] R. D. Leapman, L. A. Grunes, P. L. Fejes, *Phys. Rev. B* **1982**, *26*, 614.

[187] L. Garvie, A. J. Craven, R. Brydson, *Am. Mineral.* **1994**, *79*, 411.

[188] R. Brydson, H. Sauer, W. Engel, J. M. Thomass, E. Zeitler, N. Kosugi, H. Kuroda, *J. Phys.: Condens. Matter* **1989**, *1*, 797.

[189] P. Krüger, *Phys. Rev. B* **2010**, *81*, 125121.

[190] F. M. F. de Groot, J. C. Fuggle, B. T. Thole, G. A. Sawatzky, *Phys. Rev. B* **1990**, *41*, 928.

[191] J. P. Crocombette, F. Jollet, *J. Phys.: Condens. Matter* **1994**, *6*, 10811.

[192] H. Thakur, P. Thakur, R. Kumar, N. B. Brookes, K. K. Sharma, A. P. Singh, Y. Kumar, S. Gautam, K. H. Chae, *Appl. Phys. Lett.* **2011**, *98*, 192512.

[193] R. Brydson, H. Sauer, W. Engel, F. Hofer, *J. Phys.: Condens. Matter* **1992**, *4*, 3429.

[194] J. C. Slonczewski, *J. Magn. Magn. Mater.* **1996**, *159*, L1.

[195] S. Yuasa, A. Fukushima, K. Yakushiji, T. Nozaki, M. Konoto, H. Maehara, H. Kubota, T. Taniguchi, H. Arai, H. Imamura, K. Ando, Y. Shiota, F. Bonell, Y. Suzuki, N. Shimomura, E. Kitagawa, J. Ito, S. Fujita, K. Abe, K. Nomura, H. Noguchi, H. Yoda, in *2013 IEEE Int. Electron Devices Meeting*, IEEE **2013**, pp. 3.1.1–3.1.4.

[196] A. Uldry, F. Vernay, B. Delley, *Phys. Rev. B* **2012**, *85*, 125133.

[197] X. J. Wang, I. A. Buyanova, F. Zhao, D. Lagarde, A. Balocchi, X. Marie, C. W. Tu, J. C. Harmand, W. M. Chen, *Nat. Mater.* **2009**, *8*, 198.

[198] C. T. Nguyen, A. Balocchi, D. Lagarde, T. T. Zhang, H. Carrere, S. Mazzucato, P. Barate, E. Galopin, J. Gierak, E. Bourhis, J. C. Harmand, T. Amand, X. Marie, *Appl. Phys. Lett.* **2013**, *103*, 052403.

[199] S. Chen, Y. Huang, D. Visser, S. Anand, I. A. Buyanova, W. M. Chen, *Nat. Commun.* **2018**, *9*, 3575.

[200] L. Botsch, I. Lorite, Y. Kumar, P. D. Esquinazi, J. Zajadacz, K. Zimmer, *ACS Appl. Electron. Mater.* **2019**, *1*, 1832.

[201] C. Rauch, W. Gehlhoff, M. R. Wagner, E. Malguth, G. Callsen, R. Kirste, B. Salameh, A. Hoffmann, S. Polarz, Y. Aksu, M. Driess, *J. Appl. Phys.* **2010**, *107*, 024311.

[202] T. S. Bjørheim, S. Erdal, K. M. Johansen, K. E. Knutsen, T. Norby, *J. Phys. Chem. C* **2012**, *116*, 23764.

[203] S. Sen, K. S. Gupta, J. M. D. Coey, *Phys. Rev. B* **2015**, *92*, 155115.

[204] P. Murugan, M. Krishnamurthy, S. N. Jaisankar, D. Samanta, A. B. Mandal, *Chem. Soc. Rev.* **2015**, *44*, 3212.

[205] T. Dietl, H. Ohno, F. Matsukura, J. Cibert, D. Ferrand, *Science* **2000**, *287*, 1019.

[206] M. Venkatesan, C. B. Fitzgerald, J. M. D. Coey, *Nature* **2004**, *430*, 630.

[207] J. Coey, *J. Appl. Phys.* **2005**, *97*, 10D313.

[208] J. M. D. Coey, M. Venkatesan, P. Stamenov, C. B. Fitzgerald, L. S. Dorneles, *Phys. Rev. B* **2005**, *72*, 024450.

[209] N. H. Hong, J. Sakai, N. Poirot, V. Brizé, *Phys. Rev. B* **2006**, *73*, 132404.

[210] A. Sundaresan, R. Bhargavi, N. Rangarajan, U. Siddesh, C. N. R. Rao, *Phys. Rev. B* **2006**, *74*, 161306.

[211] N. H. Hong, J. Sakai, W. Prellier, A. Hassini, A. Ruyter, F. Gervais, *Phys. Rev. B* **2004**, *70*, 195204.

[212] S. D. Yoon, Y. Chen, A. Yang, T. L. Goodrich, X. Zuo, D. A. Arena, K. Ziemer, C. Vittoria, V. G. Harris, *J. Phys.: Condens. Matter* **2006**, *18*, L355.

[213] M. Venkatesan, C. B. Fitzgerald, J. G. Lunney, J. M. D. Coey, *Phys. Rev. Lett.* **2004**, *93*, 177206.

[214] N. H. Hong, J. Sakai, V. Brizé, *J. Phys.: Condens. Matter* **2007**, *19*, 036219.

[215] N. H. Hon, N. Poirot, J. Sakai, *Phys. Rev. B* **2008**, *77*, 033205.

[216] C. Chappert, A. Fert, F. N. V. Dau, *Nat. Mater.* **2007**, *6*, 813.

[217] T. Kawahara, *IEEE Design Test Comput.* **2011**, *28*, 52.

[218] W. Rippard, M. Pufall, S. Kaka, T. Silva, S. Russek, J. Katine, *Phys. Rev. Lett.* **2005**, *95*, 067203.

[219] H. S. Choi, S. Y. Kang, S. J. Cho, I. Y. Oh, M. Shin, H. Park, C. Jang, B. C. Min, S. I. Kim, S. Y. Park, C. S. Park, *Sci. Rep.* **2014**, *4*, 5486.

[220] S. Miwa, S. Ishibashi, H. Tomita, T. Nozaki, E. Tamura, K. Ando, N. Mizuochi, T. Saruya, H. Kubota, K. Yakushiji, T. Taniguchi, H. Imamura, A. Fukushima, S. Yuasa, Y. Suzuki, *Nat. Mater.* **2014**, *13*, 50.

[221] A. Dussaux, B. Georges, J. Grollier, V. Cros, A. V. Khvalkovskiy, A. Fukushima, M. Konoto, H. Kubota, K. Yakushiji, S. Yuasa, K. A. Zvezdin, K. Ando, A. Fert, *Nat. Commun.* **2010**, *1*, 1.

[222] C. Reig, S. Cardoso, S. C. Mukhopadhyay, *Giant Magnetoresistance (GMR) Sensors: From Basis to State-of-the-Art Applications*, Springer, New York **2014**.

[223] P. Tartaj, M. P. Morales, T. Gonzalez-Carreno, S. Veintemillas-Verdaguer, C. J. Serna, *J. Magn. Magn. Mater.* **2005**, *290–291*, 28.

[224] G. Binasch, P. Grünberg, F. Saurenbach, W. Zinn, *Phys. Rev. B* **1989**, *39*, 4828.

[225] M. N. Baibich, J. M. Broto, A. Fert, F. N. Van Dau, F. Petroff, P. Etienne, G. Creuzet, A. Friederich, J. Chazelas, *Phys. Rev. Lett.* **1988**, *61*, 2472.

[226] S. Mangin, D. Ravelosona, J. A. Katine, M. J. Carey, B. D. Terris, E. E. Fullerton, *Nat. Mater.* **2006**, *5*, 210.

[227] D. Yi, C. L. Flint, P. P. Balakrishnan, K. Mahalingam, B. Urwin, A. Vailionis, A. T. N'Diaye, P. Shafer, E. Arenholz, Y. Choi, K. H. Stone, J. H. Chu, B. M. Howe, J. Liu, I. R. Fisher, Y. Suzuki, *Phys. Rev. Lett.* **2017**, *119*, 077201.

[228] L. Liu, C. F. Pai, Y. Li, H. W. Tseng, D. C. Ralph, R. A. Buhrman, *Science* **2012**, *336*, 555.

[229] S. Emori, U. Bauer, S. M. Ahn, E. Martinez, G. S. D. Beach, *Nat. Mater.* **2013**, *12*, 611.

[230] L. Yin, X. Wang, W. Mi, *J. Appl. Phys.* **2018**, *123*, 033905.

[231] F. J. A. den Broeder, W. Hoving, P. J. H. Bloemen, *J. Magn. Magn. Mater.* **1991**, *93*, 562.

[232] F. J. A. den Broeder, H. C. Donkersloot, H. J. G. Draaisma, W. J. M. de Jonge, *J. Appl. Phys.* **1987**, *61*, 4317.

[233] P. F. Carcia, A. D. Meinhaldt, A. Suna, *Appl. Phys. Lett.* **1985**, *47*, 178.

[234] L. Berger, *Phys. Rev. B* **1996**, *54*, 9353.

[235] A. Manchon, S. Zhang, *Phys. Rev. B* **2009**, *79*, 094422.

[236] B. Dieny, M. Chshiev, *Rev. Mod. Phys.* **2017**, *89*, 025008.

[237] C. T. Rettner, S. Anders, J. E. E. Baglin, T. Thomson, B. D. Terris, *Appl. Phys. Lett.* **2002**, *80*, 279.

[238] L. F. Mattheiss, *Phys. Rev. B* **1972**, *6*, 4718.

[239] F. Bloch, G. Gentile, *Z. Phys.* **1931**, *70*, 395.

[240] H. Bethe, *Ann. Phys. (Leipzig)* **1929**, *395*, 133.

[241] L. Néel, *J. Phys. Radium* **1954**, *15*, 225.

[242] J. Zhang, Z. Zhong, X. Guan, X. Shen, J. Zhang, F. Han, H. Zhang, H. Zhang, X. Yan, Q. Zhang, L. Gu, F. Hu, R. Yu, B. Shen, J. Sun, *Nat. Commun.* **2018**, *9*, 1923.

[243] M. T. Johnson, R. Jungblut, P. J. Kelly, F. J. A. den Broeder, *J. Magn. Magn. Mater.* **1995**, *148*, 118.

[244] P. Bruno, *Phys. Rev. B* **1989**, *39*, 865.

[245] G. H. O. Daalderop, P. J. Kelly, M. F. H. Schuurmans, *Phys. Rev. B* **1994**, *50*, 9989.

[246] H. X. Yang, M. Chshiev, B. Dieny, J. H. Lee, A. Manchon, K. H. Shin, *Phys. Rev. B* **2011**, *84*, 054401.

[247] B. Rodmacq, S. Auffret, B. Dieny, S. Monso, P. Boyer, *J. Appl. Phys.* **2003**, *93*, 7513.

[248] M. T. Johnson, P. J. H. Bloemen, F. J. A. D. Broeder, J. J. D. Vries, *Rep. Prog. Phys.* **1996**, *59*, 1409.

[249] T. Liu, J. W. Cai, L. Sun, *AIP Adv.* **2012**, *2*, 032151.

[250] B. F. Vermeulen, J. Wu, J. Swerts, S. Couet, I. P. Radu, G. Groeseneken, C. Detavernier, J. K. Jochum, M. Van Bael, K. Temst, A. Shukla, S. Miwa, Y. Suzuki, K. Martens, *AIP Adv.* **2017**, *7*, 055933.

[251] H. K. Gweon, S. J. Yun, S. H. Lim, *Sci. Rep.* **2018**, *8*, 1266.

[252] B. Rodmacq, A. Manchon, C. Ducruet, S. Auffret, B. Dieny, *Phys. Rev. B* **2009**, *79*, 024423.

[253] A. Manchon, S. Pizzini, J. Vogel, V. Uhlíř, L. Lombard, C. Ducruet, S. Auffret, B. Rodmacq, B. Dieny, M. Hochstrasser, G. Panaccione, *J. Magn. Magn. Mater.* **2008**, *320*, 1889.

[254] A. Manchon, C. Ducruet, L. Lombard, S. Auffret, B. Rodmacq, B. Dieny, S. Pizzini, J. Vogel, V. Uhlíř, M. Hochstrasser, G. Panaccione, *J. Appl. Phys.* **2008**, *104*, 043914.

[255] A. Manchon, S. Pizzini, J. Vogel, V. Uhlíř, L. Lombard, C. Ducruet, S. Auffret, B. Rodmacq, B. Dieny, M. Hochstrasser, G. Panaccione, *J. Appl. Phys.* **2008**, *103*, 07A912.

[256] A. J. Schellekens, A. van den Brink, J. H. Franken, H. J. M. Swagten, B. Koopmans, *Nat. Commun.* **2012**, *3*, 847.

[257] I. M. Miron, T. Moore, H. Szambolics, L. D. Buda-Prejbeanu, S. Auffret, B. Rodmacq, S. Pizzini, J. Vogel, M. Bonfim, A. Schuhl, G. Gaudin, *Nat. Mater.* **2011**, *10*, 419.

[258] S. S. P. Parkin, M. Hayashi, L. Thomas, *Science* **2008**, *320*, 190.

[259] Y. Shiota, T. Maruyama, T. Nozaki, T. Shinjo, M. Shiraishi, Y. Suzuki, *Appl. Phys. Express* **2009**, *2*, 063001.

[260] Y. Shiota, T. Nozaki, F. Bonell, S. Murakami, T. Shinjo, Y. Suzuki, *Nat. Mater.* **2012**, *11*, 39.

[261] M. Weisheit, S. Fähler, A. Marty, Y. Souche, C. Poinsignon, D. Givord, *Science* **2007**, *315*, 349.

[262] S. Zhou, E. Čižmár, K. Potzger, M. Krause, G. Talut, M. Helm, J. Fassbender, S. A. Zvyagin, J. Wosnitza, H. Schmidt, *Phys. Rev. B* **2009**, *79*, 113201.

[263] M. M. Cruz, R. C. D. Silva, N. Franco, M. Godinho, *J. Phys.: Condens. Matter* **2009**, *21*, 206002.

[264] D. X. Li, X. B. Qin, L. R. Zheng, Y. X. Li, X. Z. Cao, Z. X. Li, J. Yang, B. Y. Wang, *Chin. Phys. B* **2013**, *22*, 037504.

[265] H. Peng, K. Lai, D. Kong, S. Meister, Y. Chen, X. L. Qi, S. C. Zhang, Z. X. Shen, Y. Cui, *Nat. Mater.* **2009**, *9*, 225.

[266] D. Sanyal, M. Chakrabarti, P. Nath, A. Sarkar, D. Bhowmick, A. Chakrabarti, *J. Phys. D: Appl. Phys.* **2013**, *47*, 025001.

[267] S. Wang, L. Pan, J. J. Song, W. Mi, J. J. Zou, L. Wang, X. Zhang, *J. Am. Chem. Soc.* **2015**, *137*, 2975.

[268] Q. Zhao, P. Wu, B. L. Li, Z. M. Lu, E. Y. Jiang, *J. Appl. Phys.* **2008**, *104*, 073911.

[269] A. K. Rumaiz, B. Ali, A. Ceylan, M. Boggs, T. Beebe, S. Ismat Shah, *Solid State Commun.* **2007**, *144*, 334.

[270] J. Zippel, M. Lorenz, A. Setzer, M. Rothermel, D. Spemann, P. Esquinazi, M. Grundmann, G. Wagner, R. Denecke, A. Timopheev, *J. Phys. D: Appl. Phys.* **2013**, *46*, 275002.

[271] J. Zippel, M. Lorenz, A. Setzer, G. Wagner, N. Sobolev, P. Esquinazi, M. Grundmann, *Phys. Rev. B* **2010**, *82*, 125209.

[272] C. D. Pemmaraju, S. Sanvito, *Phys. Rev. Lett.* **2005**, *94*, 217205.

1900623 (29 of 29)